J. Fluid Mech. (2006), *vol.* 563, *pp.* 43–69. © 2006 Cambridge University Press
doi:10.1017/S0022112006000917 Printed in the United Kingdom

Anisotropy, inhomogeneity and inertial-range scalings in turbulent convection

By FRANÇOIS RINCON

Observatoire Midi-Pyrénées, UMR 5572, Université Paul Sabatier et CNRS, F-31400 Toulouse, France

(Received 26 September 2005 and in revised form 25 January 2006)

This paper provides a detailed study of turbulent statistics and scale-by-scale budgets in turbulent Rayleigh–Bénard convection. It aims at testing the applicability of Kolmogorov and Bolgiano theories in the case of turbulent convection and at improving the understanding of the underlying inertial-range scalings, for which a general agreement is still lacking. Particular emphasis is laid on anisotropic and inhomogeneous effects, which are often observed in turbulent convection between two differentially heated plates. For this purpose, the SO(3) decomposition of structure functions and a method of description of inhomogeneities are used to derive inhomogeneous and anisotropic generalizations of Kolmogorov and Yaglom equations applying to Rayleigh–Bénard convection, which can be extended easily to other types of anisotropic and/or inhomogeneous flows. The various contributions to these equations are computed in and off the central plane of a convection cell using data produced by a direct numerical simulation of turbulent Boussinesq convection at $Ra = 10^6$ and $Pr = 1$ with aspect ratio $A = 5$. The analysis of the isotropic part of the Kolmogorov equation demonstrates that the shape of the third-order velocity structure function is significantly influenced by buoyancy forcing and large-scale inhomogeneities, while the isotropic part of the mixed third-order structure function $\langle(\Delta\theta)^2\Delta\boldsymbol{u}\rangle$ appearing in the Yaglom equation exhibits a clear scaling exponent 1 in a small range of scales. The magnitudes of the various low ℓ degree anisotropic components of the equations are also estimated and are shown to be comparable to their isotropic counterparts at moderate to large scales. The analysis of anisotropies notably reveals that computing reduced structure functions (structure functions computed at fixed depth for correlation vectors $\boldsymbol{r}$ lying in specific planes only) in order to reveal scaling exponents predicted by isotropic theories is misleading in the case of fully three-dimensional turbulence in the bulk of a convection cell, since such quantities involve linear combinations of different ℓ components which are not negligible in the flow. This observation also indicates that using single-point measurements together with the Taylor hypothesis in the particular direction of a mean flow to test the predictions of asymptotic dimensional isotropic theories of turbulence or to calculate intermittency corrections to these theories may lead to significant bias for mildly anisotropic three-dimensional flows. A qualitative analysis is finally used to show that the influence of buoyancy forcing at scales smaller than the Bolgiano scale is likely to remain important up to $Ra = 10^9$, thus preventing Kolmogorov scalings from showing up in convective flows at lower Rayleigh numbers.

1. Introduction

The quest for inertial range scaling laws in turbulent convection has been very active in recent years (e.g. Chillá *et al.* 1993; Benzi *et al.* 1994; Calzavarini *et al.*

2002; Verzicco & Camussi 2003; Ching *et al.* 2004). Their determination is expected to give some important insight into the thermal and mechanical processes at work in the flow. To this end, turbulent thermal convection is investigated in convection cells heated from below using laboratory and numerical experiments, within the framework of the Boussinesq approximation. Such a flow exhibits two essential properties: it is both strongly anisotropic and inhomogeneous. Anisotropy comes from gravity, while inhomogeneity results from the presence of top and bottom horizontal boundaries in convection cells. As a consequence, inertial-range scalings of convective turbulence, when they can ever be observed, depend strongly on the vertical coordinate.

Accordingly, asymptotic theories of turbulence constructed under the assumptions of homogeneity and isotropy may be partially irrelevant to understanding the observed properties of turbulent convection. Neglecting intermittency effects, the classical picture regarding scaling laws in this flow is that Bolgiano–Obukhov turbulence (Bolgiano 1959; Obukhov 1959, hereinafter BO59 theory) should be present on correlation lengths r larger than the so-called Bolgiano length. A dimensional estimate of this length (Chillá *et al.* 1993) is given by

$$L_B = \frac{Nu^{1/2} d}{(RaPr)^{1/4}}, \tag{1.1}$$

where d is the depth of the convective layer, Nu is the Nusselt number, Ra is the Rayleigh number and Pr is the Prandtl number. Instead, homogeneous and isotropic Kolmogorov turbulence (Kolmogorov 1941, herein after K41 theory) should be observed for $r < L_B$. In the Bolgiano–Obukhov subrange, a dominant balance between buoyancy forcing (for an unstably stratified layer) and the third-order structure function occurs, which modifies the turbulent energy cascade substantially in comparison to K41; while longitudinal velocity increment scalings $\langle \Delta u_r(r) \rangle \sim r^{1/3}$ are predicted asymptotically in the inertial range for K41, they should follow $\langle \Delta u_r(r) \rangle \sim r^{3/5}$ in the BO59 regime. As far as temperature increments are concerned, $\langle \Delta\theta(r) \rangle \sim r^{1/3}$ results from K41 (passive scalar scalings), while $\langle \Delta\theta(r) \rangle \sim r^{1/5}$ is expected from dimensional arguments in BO59 theory. These different regimes should in principle be detected through the measurements of structure functions or spectra when turbulence is sufficiently developed. However, clear evidences of K41 or BO59 scalings are still lacking in both numerical and experimental convection, even at very high Rayleigh numbers. Mixed scalings, which are not compatible with dimensional analysis, have sometimes been detected (e.g. K41 scalings for the velocity and BO59 scalings for temperature in the same wavenumber range, see for instance Verzicco & Camussi 2003). BO59 scalings have been reported in the bulk of experimental convection cells (Benzi *et al.* 1994; Ching *et al.* 2004), and in a numerical experiment (Calzavarini *et al.* 2002), close to the horizontal walls of the convection cell. Direct scaling laws could not be observed for reduced structure functions (structure functions computed at fixed depth for correlation vectors $\boldsymbol{r}$ lying in horizontal planes only) in the latter study, so that the derivation of scaling exponents by Calzavarini *et al.* (2002) relies on extended self-similarity (ESS, see Benzi *et al.* 1993). Results obtained for various anisotropic flows, such as the channel flow (Arad *et al.* 1999*a*), demonstrate that it is sometimes possible to observe scaling laws by plotting structure functions directly, even at modest Reynolds numbers, provided that the complete computation and SO(3) decomposition of structure functions are performed; in the work of Arad *et al.* (1999*a*), the difference between reduced structure functions and the isotropic (angular mean) component of the complete structure functions is striking. This spherical harmonics decomposition of structure functions has also been

computed by Biferale *et al.* (2003) for homogeneous Rayleigh–Bénard convection (HRB) in a regime where L_B is comparable to the box size, thus preventing any possibility of BO59 scalings. The anisotropic scaling exponents reported for HRB are anomalous, which means that they do not match dimensional analysis predictions either. The understanding of inertial range scalings in convective turbulence and their very existence even at high Rayleigh numbers therefore remains a puzzling problem that still deserves important efforts.

This paper aims to present a complete description of turbulent statistics in Boussinesq convection at $Ra = 10^6$ and $Pr = 1$ in order to test explicitly the assumptions of both K41 and BO59 theories in such a flow and to try to clarify some of the previously mentioned problems regarding the occurrence of inertial range scaling laws in convective turbulence. The study shows that inhomogeneity, anisotropy and the presence of buoyancy forcing at all scales all contribute to the absence of scaling laws, and points out that very high Rayleigh numbers should be reached in order to be able to observe the definite signature of spectral scalings in turbulent convection. The presentation of the results is as follows. The SO(3) decomposition of statistical averages is first used in § 2 to derive generalized Kolmogorov and Yaglom equations including inhomogeneous and anisotropic terms, which describe, respectively, the production, transport and dissipation of velocity and temperature fluctuations. A detailed numerical study of these equations is then proposed using direct numerical simulation (DNS) data. The DNS and data processing algorithms are first described in § 3. The various contributions to the equations are then presented in § 4 at the centre of the convection cell and off the central plane, with particular emphasis laid on the anisotropic and inhomogeneous effects inferred from the analysis. The consequences and perspectives offered by these results are finally discussed in § 5.

2. Theoretical considerations

Under the assumptions of homogeneity and isotropy, Kolmogorov (1941) derived his famous equation for the third-order structure function of the turbulent velocity field

$$\langle (\Delta u_r)^3 \rangle = -\tfrac{4}{5} \langle \varepsilon \rangle r + 6\nu \frac{\partial}{\partial r} \langle (\Delta u_r)^2 \rangle, \tag{2.1}$$

which leads to the well-known K41 scaling law in the inertial range of turbulence. To obtain it, one also has to assume that the forcing mechanism of turbulence is important on large scales only. There are, however, numerous flows, such as Rayleigh–Bénard convection, where some of these assumptions possibly break down. A detailed study of scale-by-scale energy budgets in turbulent convection is therefore required to test explicitly the accuracy of these assumptions. Indeed, the velocity budget will differ significantly from equation (2.1) if one or several of these hypotheses are violated. The objective of this section is to provide a derivation of generalized forms of Kolmogorov and Yaglom equations including anisotropic and inhomogeneous effects, in order to be able to perform comparisons with equation (2.1) and with the homogeneous and isotropic version of the Yaglom equation, for a given convective flow. A procedure inspired by Monin & Yaglom (1975), Lindborg (1996), Hill (1997), Antonia *et al.* (1997) and Hill (2002), is adopted here. The method has already been applied to channel flow turbulence (Danaila *et al.* 2001), heated decaying turbulence (Danaila *et al.* 1999) and shear turbulence (Casciola *et al.* 2003), which, as Rayleigh–Bénard convection, are anisotropic (and sometimes inhomogeneous) flows. Inhomogeneity is investigated in a similar fashion to Danaila *et al.* (2001). The procedure is

supplemented by a spherical harmonics decomposition of structure functions (Arad, L'vov & Procaccia 1999*b*) which serves to quantify anisotropic effects. It should be noted that a study of structure function scalings in turbulent convection is available (Yakhot 1992) and that it has been used by several authors (e.g. Benzi, Toschi & Tripiccione 1998) to predict scaling behaviour in numerical experiments. However, this work assumes isotropy and homogeneity, which, as will be shown later, are not appropriate for this flow.

2.1. *Derivation of the inhomogeneous Kolmogorov and Yaglom equations*

Summation over repeated indices is assumed throughout the derivation. A Boussinesq fluid of constant density ρ, kinematic viscosity ν and thermal diffusivity κ is used. Gravity is denoted by $\boldsymbol{g}=-g\boldsymbol{e}_z$, where z is the vertical coordinate. The Boussinesq equations (Chandrasekhar 1961) for the velocity field $\boldsymbol{u}$, pressure field p and temperature field T (separated into a mean part $\langle T\rangle$ and fluctuations θ) read

$$\partial_t u_i + u_k\partial_k u_i = -\frac{1}{\rho}\partial_i p + \alpha g\,\theta\,\delta_{iz} + \nu\partial_k^2 u_i, \tag{2.2}$$

$$\partial_t\langle T\rangle + \partial_t\theta + u_k\partial_k\theta + u_z\partial_z\langle T\rangle = \kappa\partial_k^2\theta + \kappa\partial_z^2\langle T\rangle, \tag{2.3}$$

$$\partial_k u_k = 0, \tag{2.4}$$

at position $\boldsymbol{x}$, and

$$\partial_t u_i' + u_k'\partial_k' u_i' = -\frac{1}{\rho}\partial_i' p' + \alpha g\,\theta'\,\delta_{iz} + \nu\partial_k'^2 u_i', \tag{2.5}$$

$$\partial_t\langle T'\rangle + \partial_t\theta' + u_k'\partial_k'\theta' + u_z'\partial_z'\langle T'\rangle = \kappa\partial_k'^2\theta' + \kappa\partial_z'^2\langle T'\rangle, \tag{2.6}$$

$$\partial_k' u_k' = 0, \tag{2.7}$$

at position $\boldsymbol{x}'$ (primes denote quantities evaluated at $\boldsymbol{x}'$). As is usual in this kind of analysis, $\boldsymbol{x}$ and $\boldsymbol{x}'$ are independent variables so that $\partial_k u_i' = \partial_k' u_i = 0$. Subtraction of equations (2.2) from (2.5) and (2.3) from (2.6) thus leads to

$$\partial_t\Delta u_i + \Delta u_k\partial_k'\Delta u_i + u_k(\partial_k+\partial_k')\Delta u_i = -\frac{1}{\rho}(\partial_i+\partial_i')\Delta p + \alpha g\,\Delta\theta\,\delta_{iz} + \nu\left(\partial_k^2+\partial_k'^2\right)\Delta u_i, \tag{2.8}$$

$$\begin{aligned}\partial_t\Delta\langle T\rangle + \partial_t\Delta\theta + \Delta u_k\partial_k'\Delta\theta + u_k(\partial_k+\partial_k')\Delta\theta + u_z'\partial_z'\langle T'\rangle - u_z\partial_z\langle T\rangle \\ = \kappa\left(\partial_k^2+\partial_k'^2\right)\Delta\theta + \kappa\left(\partial_z'^2\langle T'\rangle - \partial_z^2\langle T\rangle\right),\end{aligned} \tag{2.9}$$

where $\Delta f = f' - f$ for any variable f. Multiplying equations (2.8) and (2.9) by $2\Delta u_i$ and $2\Delta\theta$, respectively, using incompressibility and averaging gives

$$\begin{aligned}\partial_t\langle(\Delta u_i)^2\rangle + \langle\partial_k'(\Delta u_k(\Delta u_i)^2)\rangle + \langle(\partial_k+\partial_k')(u_k(\Delta u_i)^2)\rangle = -\frac{2}{\rho}\langle(\partial_i+\partial_i')(\Delta u_i\Delta p)\rangle \\ + 2\alpha g\,\langle\Delta\theta\Delta u_z\rangle + \nu\left\langle\left(\partial_k^2+\partial_k'^2\right)(\Delta u_i)^2\right\rangle - 2(\langle\varepsilon\rangle+\langle\varepsilon'\rangle),\end{aligned} \tag{2.10}$$

$$\begin{aligned}\partial_t\langle(\Delta\theta)^2\rangle + \langle\partial_k'(\Delta u_k(\Delta\theta)^2)\rangle + \langle(\partial_k+\partial_k')(u_k(\Delta\theta)^2)\rangle + 2\langle u_z'\partial_z'\langle T'\rangle\Delta\theta\rangle \\ - 2\langle u_z\partial_z\langle T\rangle\Delta\theta\rangle = \kappa\left\langle\left(\partial_k^2+\partial_k'^2\right)(\Delta\theta)^2\right\rangle - 2(\langle N\rangle+\langle N'\rangle),\end{aligned} \tag{2.11}$$

where $\langle\varepsilon\rangle = \nu\langle(\partial_i u_j)^2\rangle$ and $\langle N\rangle = \kappa\langle(\partial_i\theta)^2\rangle$. Following Hill (2002), the analysis can be pushed further by using new variables $\boldsymbol{X} = (\boldsymbol{x}+\boldsymbol{x}')/2$ and $\boldsymbol{r} = \boldsymbol{x}' - \boldsymbol{x}$. Differential

operators transform according to

$$\left.\begin{aligned}\partial_k &= -\frac{\partial}{\partial r_k} + \frac{1}{2}\frac{\partial}{\partial X_k},\\ \partial'_k &= \frac{\partial}{\partial r_k} + \frac{1}{2}\frac{\partial}{\partial X_k}.\end{aligned}\right\} \tag{2.12}$$

As the Rayleigh–Bénard flow is homogeneous in the horizontal directions, the $\boldsymbol{X}$ dependence is restricted to Z, so that only ∂_Z derivatives have to be considered. It is important to outline that ∂_Z is not the same operator as ∂_z, since $\boldsymbol{r}$ is to be kept constant when the former is applied, whereas z' must be kept constant in the latter case. Assuming statistical stationarity, equations (2.10)–(2.11) become

$$\begin{aligned}&\frac{\partial}{\partial r_k}\langle \Delta u_k (\Delta u_i)^2\rangle + \frac{1}{2}\frac{\partial}{\partial Z}\langle \Delta u_z (\Delta u_i)^2\rangle + \frac{\partial}{\partial Z}\langle u_z (\Delta u_i)^2\rangle = -2(\langle\varepsilon\rangle + \langle\varepsilon'\rangle)\\ &\quad - \frac{2}{\rho}\frac{\partial}{\partial Z}\langle \Delta u_z \Delta p\rangle + 2\alpha g\,\langle \Delta u_z \Delta\theta\rangle + 2\nu\frac{\partial^2}{\partial r_k^2}\langle (\Delta u_i)^2\rangle + \frac{\nu}{2}\frac{\partial^2}{\partial Z^2}\langle (\Delta u_i)^2\rangle, \qquad (2.13)\\ &\frac{\partial}{\partial r_k}\langle \Delta u_k (\Delta\theta)^2\rangle + \frac{1}{2}\frac{\partial}{\partial Z}\langle \Delta u_z (\Delta\theta)^2\rangle + \frac{\partial}{\partial Z}\langle u_z (\Delta\theta)^2\rangle + 2\langle u'_z \partial'_z \langle T'\rangle \Delta\theta\rangle\\ &\quad - 2\langle u_z \partial_z \langle T\rangle \Delta\theta\rangle = -2(\langle N\rangle + \langle N'\rangle) + 2\kappa\frac{\partial}{\partial r_k}\langle (\Delta\theta)^2\rangle + \frac{\kappa}{2}\frac{\partial^2}{\partial Z^2}\langle (\Delta\theta)^2\rangle, \qquad (2.14)\end{aligned}$$

where all quantities now depend on $(Z, \boldsymbol{r})$.

2.2. *Dealing with anisotropy*

To analyse the effects of anisotropy, a decomposition of the $\boldsymbol{r}$-dependence of statistical averages on spherical harmonics must be performed (Arad *et al.* 1999*b*). For scalar averages, denoted here by $\langle F\rangle$, such as $\langle (\Delta u_i)^2\rangle$, this decomposition reads

$$\langle F\rangle (Z, \boldsymbol{r}) = \sum_{\ell=0}^{+\infty}\sum_{m=-\ell}^{+\ell} \langle F\rangle_m^\ell (Z, r) Y_\ell^m(\theta, \varphi),$$

where $Y_\ell^m(\theta, \varphi)$ denotes the spherical harmonic of degree ℓ and azimuthal order m (here, θ denotes the angle between the vertical direction z and $\boldsymbol{r}$ and should not be confused with a temperature perturbation). One also has to deal with the vectorial averages $\langle \boldsymbol{U}\rangle \equiv \langle (\Delta u_i)^2 \Delta \boldsymbol{u}\rangle$ and $\langle \boldsymbol{\Theta}\rangle \equiv \langle (\Delta\theta)^2 \Delta \boldsymbol{u}\rangle$ appearing in equations (2.13)–(2.14). The spherical harmonics representations of these vectors are

$$\begin{aligned}\langle \boldsymbol{U}\rangle (Z, \boldsymbol{r}) = \sum_{\ell=0}^{+\infty}\sum_{m=-\ell}^{+\ell} &\langle U_R\rangle_m^\ell (Z, r)\boldsymbol{R}_\ell^m(\theta, \varphi)\\ &+ \langle U_S\rangle_m^\ell (Z, r)\boldsymbol{S}_\ell^m(\theta, \varphi) + \langle U_T\rangle_m^\ell (Z, r)\boldsymbol{T}_\ell^m(\theta, \varphi),\\ \langle \boldsymbol{\Theta}\rangle (Z, \boldsymbol{r}) = \sum_{\ell=0}^{+\infty}\sum_{m=-\ell}^{+\ell} &\langle \Theta_R\rangle_m^\ell (Z, r)\boldsymbol{R}_\ell^m(\theta, \varphi)\\ &+ \langle \Theta_S\rangle_m^\ell (Z, r)\boldsymbol{S}_\ell^m(\theta, \varphi) + \langle \Theta_T\rangle_m^\ell (Z, r)\boldsymbol{T}_\ell^m(\theta, \varphi),\end{aligned}$$

where $\boldsymbol{R}_\ell^m = Y_\ell^m \boldsymbol{e}_r$, $\boldsymbol{S}_\ell^m = \nabla Y_\ell^m$, $\boldsymbol{T}_\ell^m = \nabla \times \boldsymbol{R}_\ell^m$, and ∇ is defined at $r = 1$. $\langle U_R\rangle_m^\ell$ and $\langle U_S\rangle_m^\ell$ are the components of a vector projected directly onto a spherical harmonics

vectorial basis. They are in that sense different from a quantity such as $\langle \Delta u_z \Delta\theta \rangle_m^\ell$, which results from a projection on $\boldsymbol{e}_z$ followed by a projection on spherical harmonics. However, note that $\langle U_R \rangle_m^\ell$ could be denoted $\langle (\Delta u_i)^2 \Delta u_r \rangle_m^\ell$ as well, since $\boldsymbol{R}_\ell^m$ is along $\boldsymbol{e}_r$.

As the spherical harmonics form an orthogonal basis, equations for different ℓ and m can be considered separately. Also, a dependence of statistical averages on Z and r only will be assumed from now on and the (Z, r) notation will be omitted subsequently. Using this formalism, the divergence operator acting for instance on $\langle \boldsymbol{U} \rangle$ reads

$$\left(\frac{\partial \langle U_k \rangle}{\partial r_k} \right)_m^\ell = \frac{1}{r^2} \frac{\partial}{\partial r} \left(r^2 \langle U_R \rangle_m^\ell \right) - \frac{\ell(\ell+1)}{r} \langle U_S \rangle_m^\ell,$$

while the Laplacian of a scalar average is given by

$$\left(\frac{\partial^2 \langle F \rangle}{\partial r_k^2} \right)_m^\ell = \frac{1}{r^2} \frac{\partial}{\partial r} \left(r^2 \frac{\partial}{\partial r} \langle F \rangle_m^\ell \right) - \frac{\ell(\ell+1)}{r^2} \langle F \rangle_m^\ell.$$

Projecting equations (2.13)–(2.14) onto Y_ℓ^m for all ℓ and m and applying the operator $(1/r^2) \int_0^r y^2 \cdot \mathrm{d}y$ to the result, the following hierarchy of equations is readily obtained:

$$\begin{aligned} \langle U_R \rangle_m^\ell - \frac{\ell(\ell+1)}{r^2} \int_0^r y \langle U_S \rangle_m^\ell \, \mathrm{d}y = & -\frac{2}{r^2} \int_0^r y^2 [\langle \varepsilon \rangle + \langle \varepsilon' \rangle]_m^\ell \, \mathrm{d}y + \frac{2\alpha g}{r^2} \int_0^r y^2 \langle \Delta u_z \Delta\theta \rangle_m^\ell \, \mathrm{d}y \\ & + 2\nu \frac{\partial}{\partial r} \langle (\Delta u_i)^2 \rangle_m^\ell - \frac{2\nu \, \ell(\ell+1)}{r^2} \int_0^r \langle (\Delta u_i)^2 \rangle_m^\ell \, \mathrm{d}y \\ & + \langle NH_\nu \rangle_m^\ell + \langle NH_p \rangle_m^\ell + \langle NH_{u_z} \rangle_m^\ell + \langle NH_{\Delta u_z} \rangle_m^\ell, \end{aligned} \tag{2.15}$$

$$\begin{aligned} \langle \Theta_R \rangle_m^\ell - \frac{\ell(\ell+1)}{r^2} \int_0^r y \, \langle \Theta_S \rangle_m^\ell \, \mathrm{d}y = & -\frac{2}{r^2} \int_0^r y^2 [\langle N \rangle + \langle N' \rangle]_m^\ell \, \mathrm{d}y \\ & + \frac{2}{r^2} \int_0^r y^2 \left(\langle u_z \partial_z \langle T \rangle \Delta\theta \rangle_m^\ell - \langle u_z' \partial_z' \langle T' \rangle \, \Delta\theta \rangle_m^\ell \right) \mathrm{d}y \\ & + 2\kappa \frac{\partial}{\partial r} \langle (\Delta\theta)^2 \rangle_m^\ell - \frac{2\kappa \, \ell(\ell+1)}{r^2} \int_0^r \langle (\Delta\theta)^2 \rangle_m^\ell \, \mathrm{d}y \\ & + \left\langle NH_\kappa^\theta \right\rangle_m^\ell + \left\langle NH_{u_z}^\theta \right\rangle_m^\ell + \left\langle NH_{\Delta u_z}^\theta \right\rangle_m^\ell. \end{aligned} \tag{2.16}$$

In these equations, the inhomogeneous terms have been separated using the following notations:

$$\begin{aligned} \langle NH_\nu \rangle_m^\ell &= \frac{\nu}{2r^2} \int_0^r y^2 \frac{\partial^2}{\partial Z^2} \langle (\Delta u_i)^2 \rangle_m^\ell \, \mathrm{d}y, \\ \langle NH_p \rangle_m^\ell &= -\frac{2}{\rho r^2} \int_0^r y^2 \frac{\partial}{\partial Z} \langle \Delta u_z \Delta p \rangle_m^\ell \, \mathrm{d}y, \\ \langle NH_{u_z} \rangle_m^\ell &= -\frac{1}{r^2} \int_0^r y^2 \frac{\partial}{\partial Z} \langle u_z (\Delta u_i)^2 \rangle_m^\ell \, \mathrm{d}y, \\ \langle NH_{\Delta u_z} \rangle_m^\ell &= -\frac{1}{2r^2} \int_0^r y^2 \frac{\partial}{\partial Z} \langle \Delta u_z (\Delta u_i)^2 \rangle_m^\ell \, \mathrm{d}y \end{aligned}$$

and

$$\left\langle NH_\kappa^\theta \right\rangle_m^\ell = \frac{\kappa}{2r^2} \int_0^r y^2 \frac{\partial^2}{\partial Z^2} \langle (\Delta\theta)^2 \rangle_m^\ell \, \mathrm{d}y,$$

$$\left\langle NH^{\theta}_{u_z}\right\rangle^{\ell}_{m} = -\frac{1}{r^2}\int_0^r y^2 \frac{\partial}{\partial Z}\langle u_z(\Delta\theta)^2\rangle^{\ell}_{m}\,\mathrm{d}y,$$

$$\left\langle NH^{\theta}_{\Delta u_z}\right\rangle^{\ell}_{m} = -\frac{1}{2r^2}\int_0^r y^2 \frac{\partial}{\partial Z}\langle \Delta u_z(\Delta\theta)^2\rangle^{\ell}_{m}\,\mathrm{d}y.$$

The sums of these inhomogeneous terms in each equation will be used later on to characterize the net effect of inhomogeneity. They will be denoted by

$$\langle NH\rangle^{\ell}_{m} = \langle NH_{\nu}\rangle^{\ell}_{m} + \langle NH_{p}\rangle^{\ell}_{m} + \langle NH_{u_z}\rangle^{\ell}_{m} + \langle NH_{\Delta u_z}\rangle^{\ell}_{m},$$

$$\left\langle NH^{\theta}\right\rangle^{\ell}_{m} = \left\langle NH^{\theta}_{\kappa}\right\rangle^{\ell}_{m} + \left\langle NH^{\theta}_{u_z}\right\rangle^{\ell}_{m} + \left\langle NH^{\theta}_{\Delta u_z}\right\rangle^{\ell}_{m}.$$

The usual Kolmogorov equation, (2.1), for homogeneous and isotropic turbulence can be straightforwardly recovered from equation (2.15). Using incompressibility, and isotropy, we find that $\langle U_r\rangle = 1/(3r^3)\partial_r(r^4\langle(\Delta u_r)^3\rangle)$ and $\partial_r\langle(\Delta u_i)^2\rangle = (1/r^3)\partial_r(r^4\partial_r\langle(\Delta u_r)^2\rangle)$ (e.g. Hill 2002). Furthermore, for homogeneous and isotropic turbulence (neglecting intermittency effects), $\langle\varepsilon\rangle = \langle\varepsilon'\rangle$ and $\langle N\rangle = \langle N'\rangle$ are constants and

$$\frac{2}{r^2}\int_0^r y^2[\langle\varepsilon\rangle + \langle\varepsilon'\rangle]^{\ell}_{m}\,\mathrm{d}y = \frac{4\sqrt{4\pi}}{3}\langle\varepsilon\rangle\, r\delta^{\ell 0}\delta_{m0}, \tag{2.17}$$

$$\frac{2}{r^2}\int_0^r y^2[\langle N\rangle + \langle N'\rangle]^{\ell}_{m}\,\mathrm{d}y = \frac{4\sqrt{4\pi}}{3}\langle N\rangle\, r\delta^{\ell 0}\delta_{m0}. \tag{2.18}$$

In the preceding equations, the $\sqrt{4\pi}$ factor comes from the normalization with respect to Y_0^0. Equation (2.1) follows directly from integration of equation (2.15) by imposing $\ell = m = 0$ (isotropy) and suppressing the $\langle NH\rangle$ terms (homogeneity). As noted by several authors (e.g. Antonia *et al.* 1997), there is a striking analogy between the generalized Kolmogorov equation (2.15) which deals with the turbulent transport of kinetic energy $(\Delta u_i)^2$ and equation (2.16), which involves the turbulent transport of entropy fluctuations, which are proportional to $(\Delta\theta)^2$ for a Boussinesq fluid (L'vov 1991). This analogy is perfect when temperature is a passive scalar, while for non-neutrally stratified flows, extra terms representing the coupling between temperature and velocity fields appear.

Finally, it is worth recalling that $\langle\Delta u_z\Delta\theta\rangle^{\ell}_{m}$ stands for the projection of the scalar correlator $\langle(\Delta\boldsymbol{u}\cdot\boldsymbol{e}_z)\Delta\theta\rangle$ on Y^m_ℓ. This notation may give the impression that equation (2.15) is closed in terms of correlation functions all belonging to the same (ℓ, m) order. This is not the case because, as explained in detail by Biferale *et al.* (2003), gravity breaks the spherical symmetry of the equations of motion, leading to a coupling between the ℓ component of the Kolmogorov equation and the $(\ell-1)$, ℓ and $(\ell+1)$ harmonic components of the cross-correlator between temperature and velocity. Therefore, projecting $\langle\Delta u_z\Delta\theta\rangle$ onto Y^m_ℓ only provides a convenient way to analyse the net effect of gravity on the corresponding ℓ component of the third-order structure function and does not mean that foliation of the Rayleigh–Bénard equations with respect to ℓ (that is the question of the very existence of distinct inertial scaling exponents for different ℓ components of correlators) is satisfied. Foliation remains an open question for both Rayleigh–Bénard and Navier–Stokes equations (Biferale & Procaccia 2005).

2.3. *Symmetries of the Boussinesq equations*

Statistical averages in equations (2.15)–(2.16) obey some symmetry properties which will be listed here before a detailed analysis is carried out. First, there is an azimuthal

symmetry which is due to isotropy in horizontal planes, so that only the $m=0$ components need be considered here. The other important symmetry is the top-down symmetry of the Boussinesq equations. For $z=1/2$, the following rules can be derived:

(*a*) $\langle U_R\rangle_0^\ell$ vanishes for odd ℓ;

(*b*) the even ℓ components of statistical averages containing odd powers of u_z, such as for instance $\langle u_z(\Delta u_i)^2\rangle_0^\ell$, vanish, while their Z-derivatives are non-zero;

(*c*) the Z-derivatives of the odd ℓ components of the same statistical averages vanish.

Consequently, only even ℓ have to be considered at the centre of the cell. Except for the azimuthal symmetry, the previous rules cannot be applied to $z\neq 1/2$, where the complete ℓ spectrum has to be computed. An important consequence of the previous observations is that inhomogeneous effects should be present at the centre of the convection cell, and that the isotropic component should be affected by these effects. This also occurs for the channel flow, which obeys the same top-down symmetry (Danaila *et al.* 2001) as Boussinesq convection.

3. Numerics

The various terms in equations (2.15)–(2.16) have to be computed in order to shed some light on the dominant contributions to the third-order structure functions $\langle \boldsymbol{U}\rangle$ and $\langle \boldsymbol{\Theta}\rangle$ and to test quantitatively the assumptions of both BO59 and K41 theories for this flow. To this end, one can choose to resort to either laboratory or numerical experiments. As will be discussed shortly, the main drawback of numerics is that only moderate Rayleigh numbers can be achieved in comparison to laboratory experiments. However, many interesting benefits can be gained from using numerical simulations to study the properties of equations (2.15)–(2.16). The most important ones are that complete two-points averages can be computed easily without invoking the Taylor hypothesis and assuming isotropy, and that every quantity such as p can be easily obtained from the simulation at various locations. This motivated the choice of using numerics in the present study. A description of the DNS and numerical procedures used in order to perform this numerical analysis is now presented.

3.1. *Code set-up*

To investigate equations (2.15)–(2.16), the Boussinesq equations (2.2)–(2.3) for velocity and temperature are solved for $Ra=10^6$, $Pr=1$ and an aspect ratio $A=5$ with a DNS code initiated by Califano (1996), designed for anisotropic flows. It makes use of a sixth-order compact finite-difference scheme (Lele 1992) in the vertical z-direction and of a spectral scheme with 2/3 dealiasing in the horizontal direction. Time-stepping is implemented via a third-order fully explicit Runge–Kutta scheme (Demuren, Wilson & Carpenter 2001). A projection method is used to ensure that the velocity field remains divergence-free. This method involves a Poisson solver to compute the pressure field. For the chosen aspect ratio, 256 points are used in each horizontal direction and 128 points in the vertical. A smaller mesh size is required in the vertical to resolve the thermal boundary layers accurately. Fixed temperature and stress-free boundary conditions are imposed on both plates, while periodic boundary conditions are used in the horizontal directions. Note that these boundary conditions offer a higher supercriticality (for a given Rayleigh number) than rigid boundaries, so that this simulation at $Ra=10^6$ is in all likelihood located at the lower end (with respect to Ra) of the soft turbulence regime range of convection (Heslot, Castaing & Libchaber 1987).

Distances are normalized with respect to d: $z=0$ corresponds to the bottom plate and $z=1$ to the top one. The simulation starts from small random temperature perturbations of the initial linear temperature profile and lasts for approximately fifty turnover times of the fluid, where one turnover time, defined here as twice the time it would take for a fluid element with velocity equal to the r.m.s. vertical velocity in the central plane to travel from one boundary to the other, corresponds to the time interval required before two snapshots can be considered independent. After a short linear growth phase, an energetically steady turbulent state is reached in approximately one turnover time. It should be noted that plume clustering (Cattaneo, Lenz & Weiss 2001; Hartlep, Tilgner & Busse 2003; Parodi *et al.* 2004; Rincon, Lignières & Rieutord 2005) is observed in moderate and large aspect ratio simulations, which can be identified with the mean wind observed in small aspect ratio convection cells, as shown by van Reeuwijk, Jonker & Hanjalic (2005). The slow evolution of the integral scale towards large scales that results from this effect does not affect the results presented here, which concern structures on scales smaller than the layer depth, for which an energetically steady state is reached quickly. In the statistically steady state, the Nusselt number computed from the data of the simulation is $Nu \sim 14$. The Bolgiano scale, following equation (1.1), is $L_B = 0.11$ (with respect to d), but as will be shown later, this value does not correspond to the effective Bolgiano scale at the centre of the convection cell. The Kolmogorov dissipation scale, $\eta = 0.016$, is adequately resolved with the chosen mesh sizes. At the centre of the convection cell, the Reynolds number based on the r.m.s. velocity and the layer depth is $Re \simeq 320$ and the Taylor Reynolds number is $Re_\lambda \simeq 30$.

3.2. *Averaging procedure and statistical convergence*

Statistical averages are computed for given horizontal planes z by measuring each required quantity once every turnover time and at every four points in each horizontal direction. This procedure has notably been used by Arad *et al.* (1999*a*) for the channel flow and makes uses of homogeneity in both horizontal directions. At this stage, one may wonder why only a moderately turbulent simulation with $Ra = 10^6$ is presented here, whereas Verzicco & Camussi (2003) managed to simulate convective flows up to $Ra = 2 \times 10^{11}$. It is worth emphasizing that the present work aims at computing various two-point statistical averages, and that such computations require a very long integration of the equations and a large number of independent realizations of the flow to be collected in order to obtain a good convergence, especially for structure functions of odd order and large ℓ components. This very large data and computing-time requirement is the main reason why all numerical studies that deal with the computation of statistical quantities such as structure functions have to make an important compromise between resolution and integration time and are therefore currently limited to moderate Rayleigh/Reynolds numbers. For instance, Arad *et al.* (1999*a*) used 160 independent snapshots of their flow at $Re_\lambda = 70$ to compute structure functions, while Casciola *et al.* (2003) simulated shear flow turbulence at $Re_\lambda = 45$ during 5900 shearing times in order to perform their statistical analysis. Calzavarini *et al.* (2002) and Biferale *et al.* (2003) stored, respectively, 400 and 270 independent configurations of aspect ratio one convective turbulence at Rayleigh numbers of order 10^7. Such parameter values all lead to turbulent regimes comparable to that of this simulation (in the case of Casciola *et al.* 2003, the largest value for r is 55η, to be compared with 30η here). In the present study, convergence for all statistical quantities at correlation lengths smaller than 0.5 starts to be satisfactory (up to a few per cent) after approximately ten turnover times, which is only possible because

one time snapshot of a simulation with aspect ratio $A = 5$ can be considered ideally as 25 independent snapshots of an aspect ratio one simulation for scales smaller than 0.5. Therefore, convergence is, in fact, only obtained by collecting more than 200 independent 'aspect ratio one' snapshots, as in the previously mentioned studies. In comparison, the high-resolution simulations by Verzicco & Camussi (2003) with aspect ratio $A = 1/2$ last for at most 220 free-fall turnover times, which corresponds to only 16 turnover times as defined here. (Snapshots separated by one free-fall turnover time in their study cannot be considered independent. The free-fall turnover time in their simulation is approximately 14 times smaller than the turnover time based on the r.m.s. vertical velocity, since the latter is approximately 0.07 times the free-fall velocity (see their figure 14).) This is far from sufficient to obtain convergence for all statistical quantities of interest and, unfortunately, performing such simulations for much longer times is currently prohibitive because of the computing time required.

3.3. *SO*(3) *decomposition*

The spherical harmonics decomposition is computed in the following way: statistical averages are computed for various correlation length vectors $\boldsymbol{r}$ making different angles θ with the vertical direction, located on a Gauss–Legendre grid containing 15 points. This computation is performed for 20 different values of the azimuthal angle φ. A Fourier transform on φ and a Legendre transform on θ follow, which lead to the amplitudes of the various (ℓ, m) components at a given r. The procedure is repeated at various distances r to obtain the final results. Interpolation between grid points is the only trick that one has to resort to in order to compute anisotropic structure functions. It does not affect the results significantly except for very small correlation lengths comparable to the mesh size. The ∂_Z and ∂_Z^2 derivatives in the inhomogeneous terms are calculated by differentiating results obtained at different z with fourth-order finite-difference schemes.

4. Results

This section provides an exhaustive presentation of results obtained by computing the various terms in equations (2.15)–(2.16) from DNS data. A preliminary analysis is first carried out in order to outline inhomogeneous effects in the Rayleigh–Bénard system.

4.1. *Inhomogeneity in turbulent Rayleigh–Bénard convection*

Figure 1 represents snapshots of temperature perturbations in the midlayer and close to the surface in the statistically stationary state of the simulation. Obviously, temperature maps at different altitudes look very different: while large-scale temperature perturbations dominate the convective pattern inside the cell, smaller-scale structures separated by dark lanes become prominent in the thermal boundary layer close to the surface. The presence of these dark lanes also leads to a clear increase of small-scale power in the temperature spectra computed close to the plates (Rincon *et al.* 2005). This depth-variation of the properties of convective turbulence has been known for a long time. It is even more striking in non-Boussinesq compressible convection, where the top-down symmetry is lost (e.g. Toomre *et al.* 1990; Cattaneo *et al.* 1991). Inhomogeneity in the system is further illustrated in figure 2, which shows horizontal velocity spectra computed at various altitudes z. These spectra are defined according to

$$E(k, z) = \int_{\Omega_k} |\hat{\boldsymbol{u}}_{\boldsymbol{k}}(z)|^2 k \, \mathrm{d}\Omega_{\boldsymbol{k}}, \tag{4.1}$$

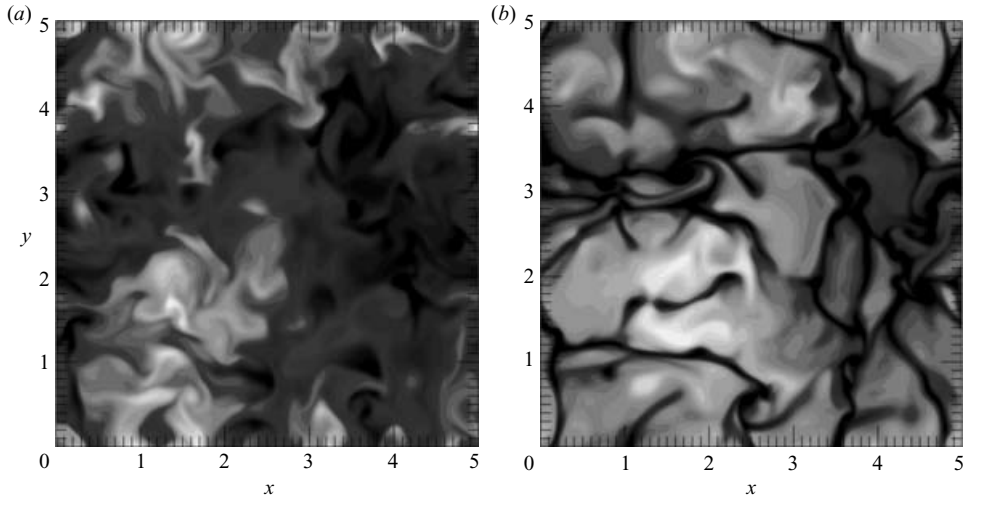

FIGURE 1. Horizontal maps of temperature fluctuations at (*a*) $z = 0.5$ and (*b*) $z = 0.9$.

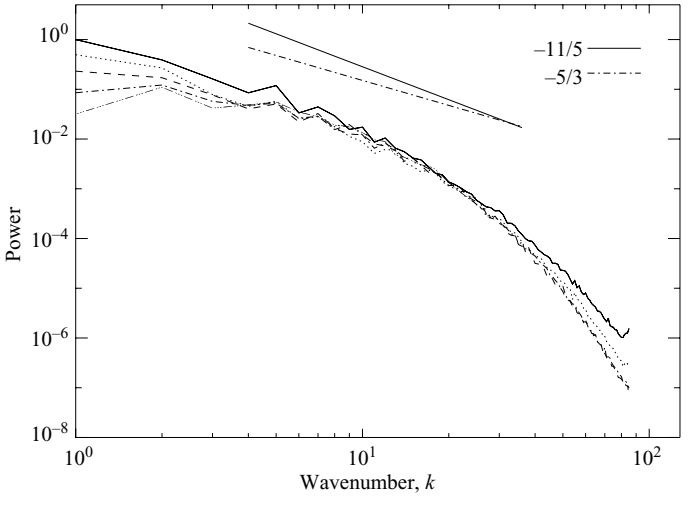

FIGURE 2. Velocity spectra defined in equation (4.1) for $z = 0$ (———), $z = 0.13$ (· · ·), $z = 0.25$ (- · -), $z = 0.38$ (— · · · —). $z = 0$ corresponds to the bottom of the convective cell. Because of the top-down symmetry of Boussinesq convection, only spectra in the lower half of the layer are presented. BO59 and K41 slopes have been overplotted to illustrate the difficulty in identifying a definite spectral slope. Wavenumbers have been normalized with respect to $2\pi/(dA)$, so that $k = 1$ corresponds to the largest horizontal scale of the domain.

where Ω_k stands for the wave vector angles in the horizontal spectral plane, and the hat denotes horizontal Fourier transforms. Measuring definite slopes on these spectra proves all the more difficult as their shapes depend strongly on the depth at which the computation is carried out. As will be demonstrated in the next sections, there are various reasons for this absence of scaling laws. Note finally that the previously mentioned small-scale structures that appear on temperature maps close to the surface are essentially temperature perturbations, which explains why they do not show up in the corresponding velocity spectra at intermediate wavenumbers.

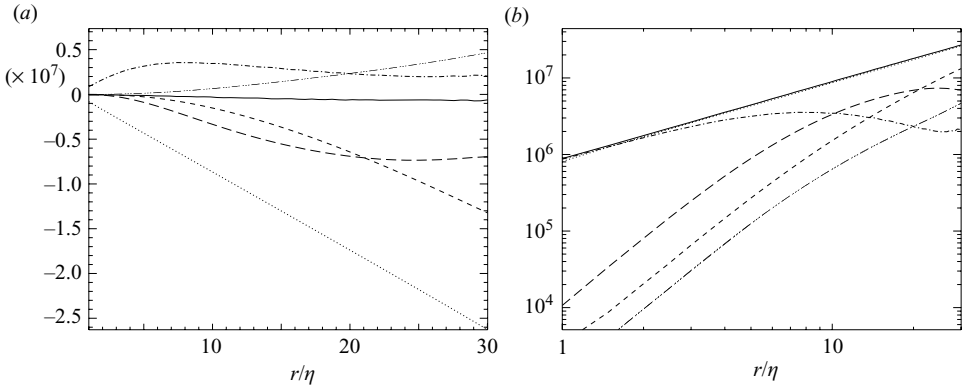

FIGURE 3. Two different representations of the scale-by-scale budget equation (4.2). (*a*) Linear-linear plots of $\langle U_R\rangle_0^0$ (— — —), $-(2\alpha g/r^2)\int_0^r y^2\langle\Delta u_z\Delta\theta\rangle_0^0\,\mathrm{d}y$ (- - -), $2\nu\partial_r\langle(\Delta u_i)^2\rangle_0^0$ (- · -), $\langle NH\rangle_0^0$ (— · · · —), $-(4/3)\langle\varepsilon\rangle r$ term (· · ·) and net budget (———). (*b*) Log–log plots of $-\langle U_R\rangle_0^0$ (— — —), $(2\alpha g/r^2)\int_0^r y^2\langle\Delta u_z\Delta\theta\rangle_0^0\,\mathrm{d}y$ (- - -), $2\nu\partial_r\langle(\Delta u_i)^2\rangle_0^0$ (- · -), $\langle NH\rangle_0^0$ (— · · · —). The sum of the left-hand side terms of equation (4.2) (———) is seen to be in very good balance with the right-hand side $(4/3)\langle\varepsilon\rangle r$ term (· · ·). $\ell = 0$.

4.2. *Isotropic component of equations* (2.15)–(2.16)

The first step in the analysis of the simulation is the examination of the isotropic parts of equations (2.15)–(2.16), which take on the following form:

$$-\langle U_R\rangle_0^0+\frac{2\alpha g}{r^2}\int_0^r y^2\langle\Delta u_z\Delta\theta\rangle_0^0\,\mathrm{d}y+2\nu\frac{\partial}{\partial r}\langle(\Delta u_i)^2\rangle_0^0+\langle NH\rangle_0^0=\frac{2}{r^2}\int_0^r y^2[\langle\varepsilon\rangle+\langle\varepsilon'\rangle]_0^0\,\mathrm{d}y, \tag{4.2}$$

$$-\langle\Theta_R\rangle_0^0+\frac{2}{r^2}\int_0^r y^2\big(\langle u_z\partial_z\langle T\rangle\Delta\theta\rangle_0^0-\langle u_z'\partial_z'\langle T'\rangle\Delta\theta\rangle_0^0\big)\,\mathrm{d}y+2\kappa\frac{\partial}{\partial r}\langle(\Delta\theta)^2\rangle_0^0$$
$$+\langle NH^\theta\rangle_0^0=\frac{2}{r^2}\int_0^r y^2[\langle N\rangle+\langle N'\rangle]_0^0\,\mathrm{d}y. \tag{4.3}$$

In the following, the right-hand sides of equations (4.2)–(4.3) will be shown to be always close to $(4\sqrt{4\pi}/3)\langle\varepsilon\rangle r$ and $(4\sqrt{4\pi}/3)\langle N\rangle r$, respectively, except on large scales r, which correspond to penetration of the correlation length vector into the boundary layers, where dissipation (and so $\langle\varepsilon'\rangle$) increases. For clarity, these terms will thus be referred to as '$(4/3)\langle\varepsilon\rangle r$' and '$(4/3)\langle N\rangle r$' terms.

4.2.1. *Central plane analysis*

Focus is first given to the central plane $z = 1/2$. An illustration of equation (4.2) at $z = 1/2$ is given in figure 3. The right-hand side of equation (4.2) is almost linear with a slope $(4\sqrt{4\pi}/3)\langle\varepsilon\rangle$. This $(4/3)\langle\varepsilon\rangle r$ term is the dominant contribution to the third-order structure function at moderate to large scales, but forcing by buoyancy is also important in the same range, as seen in figure 3(*a*). As shown by Calzavarini *et al.* (2002), the estimate of the Bolgiano length (1.1) is rather crude and the effective Bolgiano length (corresponding to the crossover between the buoyancy term and $-(4/3)\langle\varepsilon\rangle r$) at the centre of the convection cell which can be extrapolated from figure 3 is more likely to be closer to 1 ($r/\eta\simeq 60$) than to 0.1 ($r/\eta = 6$). The aspect ratio and set of boundary conditions have a direct influence on the prefactors of the various relations leading to equation (1.1) and thus affect the value of the effective

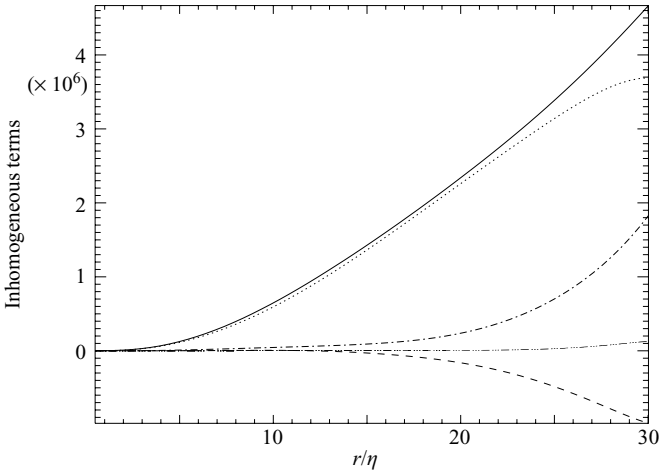

FIGURE 4. Decomposition of $\langle NH\rangle_0^0$ (———) into $\langle NH_v\rangle_0^0$ (— · · · —), $\langle NH_p\rangle_0^0$ (- · -), $\langle NH_{u_z}\rangle_0^0$ (· · ·), $\langle NH_{\Delta u_z}\rangle_0^0$ (- - -). The large-scale inhomogeneity $\langle NH_{u_z}\rangle_0^0$ dominates the overall inhomogeneous contribution to equation (4.2). $\ell = 0$.

Bolgiano length. Another simulation (not presented here) with aspect ratio 1 and all other parameters remaining constant notably reveals that L_B tends to become smaller in the central plane for convection cells with smaller aspect ratio. This effect may be related to the presence of a mean wind (plume clustering): as shown by Rincon *et al.* (2005), the scale of the mean wind corresponds to the scale at which a maximum power is injected through buoyancy. In an aspect ratio 1 simulation, these structures have to concentrate in a cube of aspect ratio 1, while they are allowed to spread over larger horizontal scales at larger aspect ratio. Buoyancy forcing may consequently be more important at smaller scales in small aspect ratio convection, thus reducing the effective Bolgiano length. Note, finally, that equation (1.1) does not take into account the fact that the Bolgiano length derived by Bolgiano and Obukhov depends on z-dependent dissipation rates and is therefore z-dependent as well. Using this exact expression, as done notably by Calzavarini *et al.* (2002), does not lead to order of magnitude changes for L_B in the bulk of the convection cell in comparison to the estimation provided by equation (1.1) for the present simulation. In fact, both expressions rely on dimensional analysis and must therefore be understood as estimations up to order one prefactors.

Using the effective value $L_B \simeq 1$ for this simulation, one can estimate that $L_B/\eta \simeq 60$, so that there should, in principle, be some room for K41 scalings to occur for $\eta < r < L_B$. However, the buoyancy term always remains of the same order of magnitude as the $-(4/3)\langle\varepsilon\rangle r$ term. Also, these two terms have opposite sign, which leads to a significant modification of the third-order structure function in comparison to isotropic turbulence forced on the largest scales only. The inhomogeneous term $\langle NH\rangle_0^0$ also gives a positive contribution that compensates the $-(4/3)\langle\varepsilon\rangle r$ term. This inhomogeneous term increases with r and becomes larger than the viscous term for $r \simeq 20\eta$. A detailed analysis of this term (figure 4) shows that the main contribution comes from $\langle NH_{u_z}\rangle_0^0$. The other inhomogeneous terms have a smaller influence on the global budget of equation (4.2). Danaila *et al.* (2001) have shown that the $\langle NH_{u_z}\rangle$ term, which they have identified as a large-scale inhomogeneity, is also the dominant inhomogeneous contribution in channel-flow turbulence.

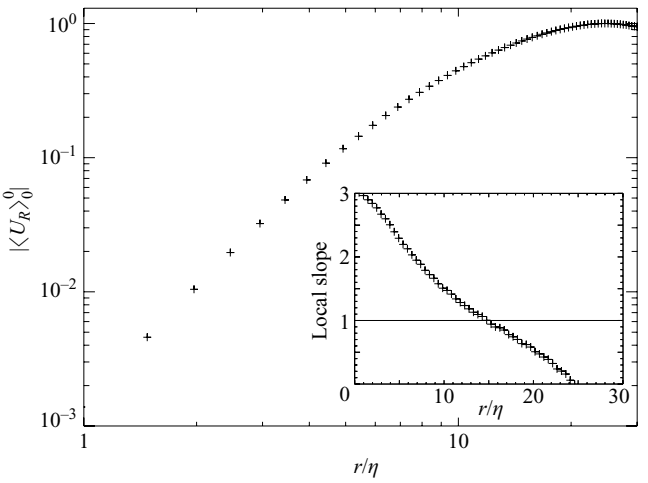

FIGURE 5. $|\langle U_R\rangle_0^0|$ as a function of r/η, normalized with respect to its maximum over r. Inset: logarithmic slope of the same function. A K41 scaling would lead to $\langle U_R\rangle_0^0 \sim r$ (up to a sign change). $\ell = 0$.

The most important consequence of having several important contributions to the third-order structure function is that it does not exhibit any scaling behaviour. To illustrate this, a plot of $\langle U_R\rangle_0^0$ is given in figure 5, together with a plot of the associated local logarithmic slope. It proves impossible to identify an inertial range on this plot, but note as a verification that the local slope of $\langle U_R\rangle_0^0$ tends to 3 at very small scales, as expected from classical arguments. It is often claimed that the absence of scaling behaviour in various flows is due to the smallness of the Reynolds number, because in that case the viscous term in equation (2.1) cannot be neglected at most scales. This is only partly true for this convective flow, since the viscous term appears to be far smaller than the $-(4/3)\langle\varepsilon\rangle r$ term for $r > 0.15$ ($r/\eta > 10$). Strictly speaking, the smallness of the Reynolds number is mainly responsible for the absence of a very large-scale separation between L_B and η here, which leads to the previously mentioned compensation effect. As will be discussed in § 5, definite scalings in the range $\eta < r < L_B$ may only be observed for very large Rayleigh numbers. In any case, in a homogeneous flow forced on large scales only, for which no compensation by a forcing mechanism exist, scalings should in principle be observed, at least in a restricted subrange. There is, however, a supplementary effect which may prevent scaling laws from showing up even in this favourable situation, namely anisotropy. In that case, the occurrence of scalings may depend on the way data is analysed. This point will be further investigated later on in the paper.

Comparing convective turbulence to other types of flow such as channel flow and shear flow shows that many features of turbulence are shared by all these flows, even though their forcing mechanisms are completely different. For instance, figure 3(*b*) can easily be compared to figure 5 of Danaila *et al.* (2001). These authors studied the effect of inhomogeneity on third-order structure functions for the channel flow by assuming isotropy, which is, however, not completely satisfied in the flow. The main difference with the channel flow is that the $\langle NH\rangle_0^0$ term does not tend to balance $-(4/3)\langle\varepsilon\rangle r$ directly in turbulent convection at the largest scales that can be analysed using the SO(3) technique, since buoyancy forcing becomes increasingly important at such scales. Instead, the inhomogeneous term tends to compensate the net effect

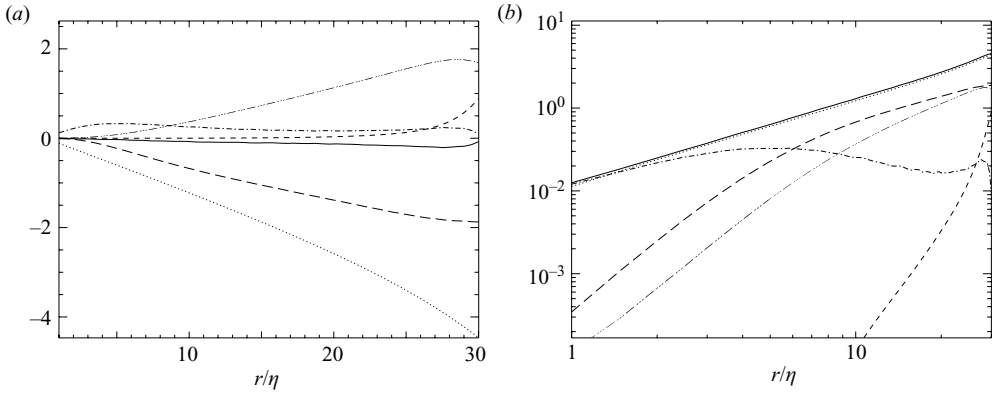

FIGURE 6. Representations of the temperature scale-by-scale budget governed by equation (4.3). (*a*) Linear–linear plots of $\langle\Theta_R\rangle_0^0$ (— — —), $(2/r^2)\int_0^r y^2(\langle u_z\partial_z\langle T\rangle\Delta\theta\rangle_0^0-\langle u_z'\partial_z'\langle T'\rangle\Delta\theta\rangle_0^0)\,\mathrm{d}y$ (- - -), $2\kappa\partial_r\langle(\Delta\theta)^2\rangle_0^0$ (- · -), $\langle NH^\theta\rangle_0^0$ (— · · · —), $-(4/3)\langle N\rangle r$ term (· · ·) and net budget (———). (*b*) Log–log plots of $-\langle\Theta_R\rangle_0^0$ (— — —), $(2/r^2)\int_0^r y^2(\langle u_z\partial_z\langle T\rangle\Delta\theta\rangle_0^0-\langle u_z'\partial_z'\langle T'\rangle\Delta\theta\rangle_0^0)\,\mathrm{d}y$ (- - -), $2\kappa\partial_r\langle(\Delta\theta)^2\rangle_0^0$ (- · -), $\langle NH^\theta\rangle_0^0$ (— · · · —). The sum of the left-hand side terms of equation (4.3) (———) is seen to be in very good balance with the right-hand side $4/3\langle N\rangle r$ term (· · ·). $\ell=0$.

of $-(4/3)\langle\varepsilon\rangle r$ and of buoyancy (note that the situation is slightly different from the previously mentioned channel-flow study, since the SO(3) analysis is restricted to scales smaller than the integral scale of the flow, so that $\langle U_R\rangle_0^0$ does not tend to zero yet at the largest scales available). Another interesting comparison with the results of Casciola *et al.* (2003) for homogeneous shear flow (their figure 1) and figure 3(*a*) can be made. Their results are restricted to $\ell=0$, since their scale-by-scale budget results from averaging structure functions over a $\boldsymbol{r}$-sphere. Except for inhomogeneous effects, the scale-by-scale budgets of the two flows are very similar. Buoyancy appears to play almost the same role in Rayleigh–Bénard convection as shear forcing in a shear flow. The same conclusions regarding the determination of structure function exponents can be drawn for both flows, since the forcing remains important at all scales in both cases.

Equation (4.3) for temperature fluctuations is also worth analysing in the central plane. Figure 6 represents the various terms in this equation in a similar way to that in figure 3. A plot of $\langle\Theta_R\rangle_0^0$ is presented in figure 7, together with the associated logarithmic local slope. A clear plateau close to value 1 is observed for the logarithmic slope for $12\eta<r<25\eta$. This plateau corresponds to a dominant balance between $\langle\Theta_R\rangle_0^0$ and the $-(4/3)\langle N\rangle r$ term, which is required in both BO59 ($r\sim(r^{3/5}\times(r^{1/5})^2)$) and K41 ($r\sim(r^{1/3}\times(r^{1/3})^2)$) theories. Figure 6 shows notably that the BO59 hypothesis which neglects advection of the mean temperature profile term in comparison to the $-(4/3)\langle N\rangle r$ term is very well satisfied in the simulation, because the core of the convection cell is almost isothermal at $Ra=10^6$, so that the $\partial_z\langle T\rangle$ terms are negligible in this region. Inhomogeneity is seen to give a significant contribution to the third-order structure function, mainly through the action of large-scale inhomogeneities $\langle NH_{u_z}^\theta\rangle_0^0$ (figure 8), as in the velocity equation. However, this does not prevent scaling behaviour in a small 'inertial' range in that case. The reason for this is that the dominant inhomogeneous term $\langle NH_{u_z}^\theta\rangle_0^0$, as can be seen on the same plot, is also proportional to r on large scales (figure 6*b*). Note that the observation of scalings for temperature related structure functions, but not for velocity structure functions, cannot simply be attributed to the present value of the Prandtl number,

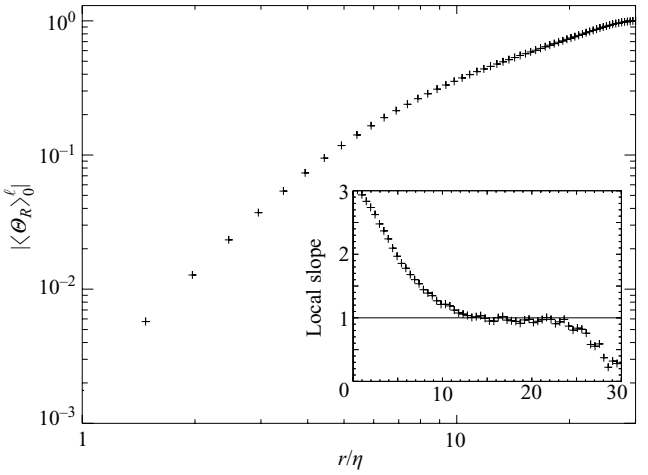

FIGURE 7. $|\langle\Theta_R\rangle_0^0|$ normalized to its maximum over r and its local logarithmic slope (inset), as a function of r/η. $\ell = 0$.

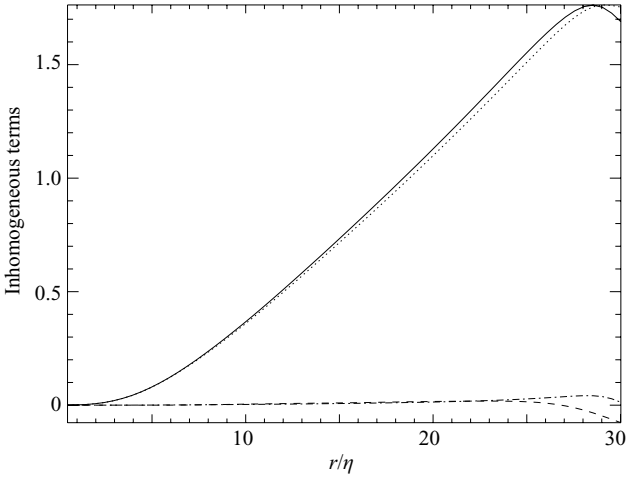

FIGURE 8. Decomposition of $\langle NH^\theta\rangle_0^0$ (———) into $\langle NH_\kappa^\theta\rangle_0^0$ (- · -), $\langle NH_{u_z}^\theta\rangle_0^0$ (· · ·), $\langle NH_{\Delta u_z}^\theta\rangle_0^0$ (- - -). As for the velocity equation, the large-scale inhomogeneity $\langle NH_{u_z}^\theta\rangle_0^0$ dominates the overall inhomogeneous contribution to equation (4.3). $\ell = 0$.

because the potential scaling ranges of $\langle U_R\rangle_0^0$ and $\langle\Theta_R\rangle_0^0$ should be similar for $Pr = 1$. This analysis therefore confirms that moderate values of the Taylor Reynolds or Péclet numbers (the equivalent of the Reynolds number for thermal diffusion) do not necessarily imply that an inertial range should not exist.

4.2.2. *Analysis off the central plane*

The main problem with the SO(3) decomposition of structure functions is that the analysis must be restricted to rather small scales r in regions close to the boundaries of the system (for wall-type boundary conditions). In such regions, the computation of reduced structure functions with $\boldsymbol{r}$ lying in planes parallel to the boundaries remains the only available tool (see Calzavarini *et al.* (2002) for an application to Rayleigh–Bénard convection). Remembering that the symmetry properties listed in § 2

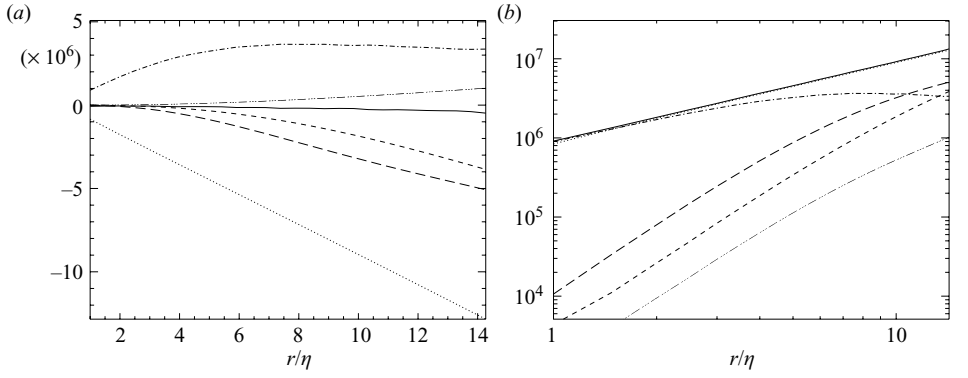

FIGURE 9. Two representations of equation (4.2) for $z = 1/4$. The legends are the same as in figure 3. $\ell = 0$.

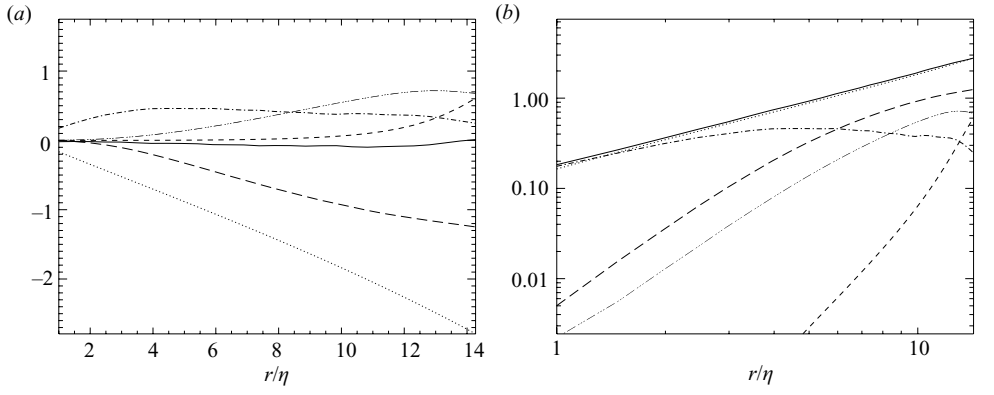

FIGURE 10. Two representations of equation (4.3) for $z = 1/4$. The legends are the same as in figure 6. $\ell = 0$.

disappear off the central plane, it is, however, interesting to push the SO(3) analysis as far as possible from this region in order to observe trends of the z-dependence of inhomogeneous effects. A brief description of turbulent statistics at $z = 1/4$ is given to this end. At this altitude, the maximum r for which turbulent statistics can be computed is only 15η, so that care must be taken in the interpretation of the results. For such a restricted range of correlation lengths, it is clear that, at most, a beginning of the inertial range can be expected and that probing inhomogeneous effects proves difficult, since these effects should be dominant on scales comparable to the integral scale of the flow only.

As can be seen in figures 9 and 10, the behaviour of the various terms in equations (4.2)–(4.3) for $r < 15\eta$ and $z = 1/4$ is not very different from the case $z = 1/2$ at first sight. There is, however, a slight difference concerning inhomogeneous effects in the velocity equation, which may be due to the closeness of the bottom wall: figure 11 reveals that normal pressure diffusion, which was small at small scales for $z = 1/2$, gives a significant contribution at the same scales for $z = 1/4$. This term is notably seen to continue to increase on the largest scales available, while $\langle NH_{u_z} \rangle_0^0$ seems to have reached a maximum for r close to the distance to the bottom boundary z. As far as the scaling of $\langle U_R \rangle_0^0$ is concerned, figure 12 shows a possible trend

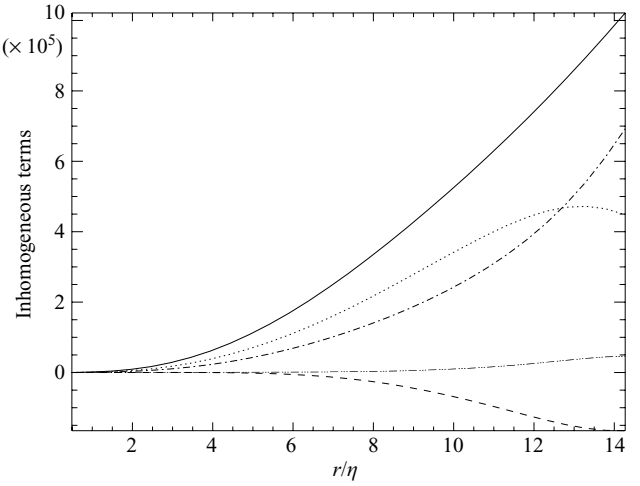

FIGURE 11. Decomposition of $\langle NH\rangle_0^0$ at $z=1/4$. Note the significant contribution of the pressure diffusion term. Same legend as in figure 4. $\ell=0$.

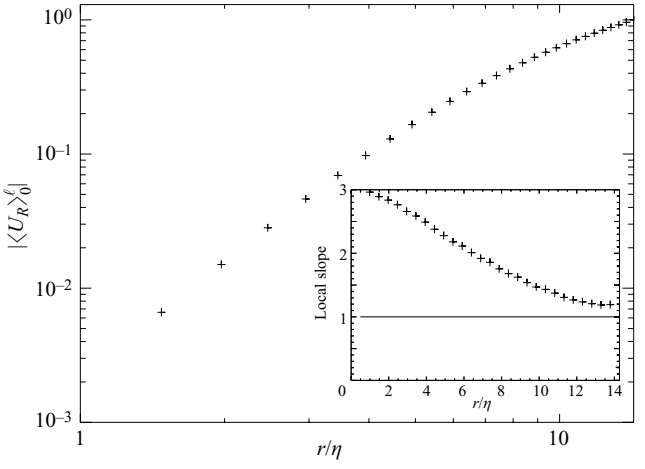

FIGURE 12. $|\langle U_R\rangle_0^0|$ normalized with respect to its maximum over r, as a function of r/η, at $z=1/4$. Inset: logarithmic slope of the same function. $\ell=0$.

towards slope 1 for $r/\eta\simeq 14$, but no real balance between the $-(4/3)\langle\varepsilon\rangle r$ term and the structure function is visible on figure 9.

Meanwhile, figure 13 reveals that the logarithmic slope of $\langle\Theta_R\rangle_0^0$, unlike for $z=1/2$, does not seem to tend to 1 at the largest scales available for $z=1/4$. Figure 14 shows that inhomogeneous effects in the temperature equation are still mainly due to the $\langle NH_{u_z}^{\theta}\rangle$ term in this region. It therefore seems difficult to make definite conclusions regarding scaling laws in this region. It can only be asserted, following figure 9, that the assumptions of homogeneity and of large-scale forcing are still clearly violated at $z=1/4$. Explaining the logarithmic slope 1 for $\langle U_R\rangle_0^0$ by simple K41 arguments therefore proves difficult in that case. This special slope may, for instance, be related to the penetration of $\boldsymbol{r}$ in the lower boundary layers where the flow dynamics are quite different from those in the bulk of the convection cell.

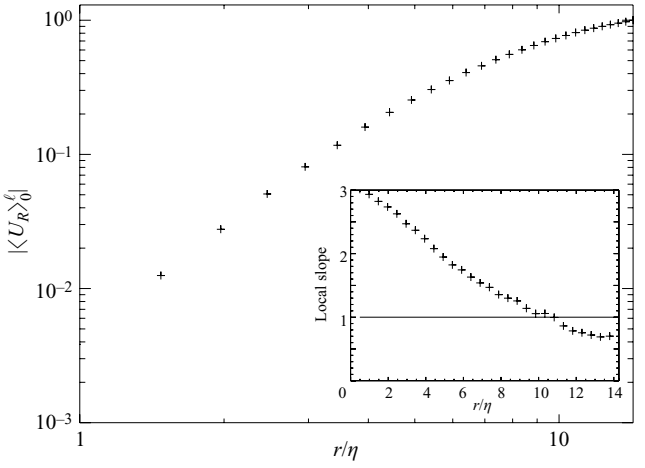

FIGURE 13. $|\langle\Theta_R\rangle_0^0|$ normalized with respect to its maximum over r and its local logarithmic slope (inset), as a function of r/η, at $z=1/4$. $\ell=0$.

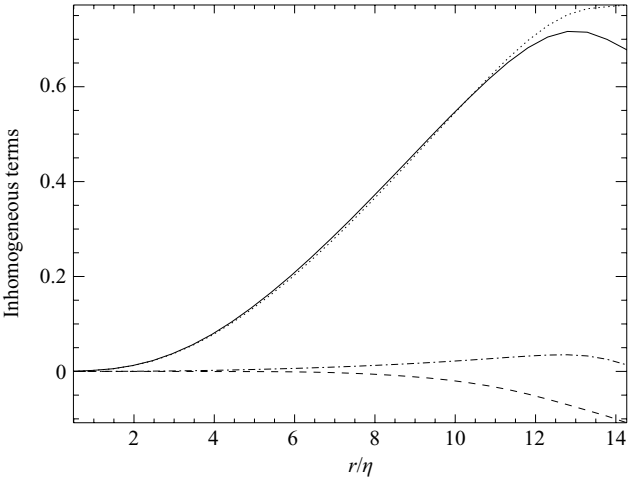

FIGURE 14. Decomposition of $\langle NH^\theta\rangle_0^0$ at $z=1/4$. Same legend as in figure 8. $\ell=0$.

4.3. *Anisotropic components*

In the preceding paragraphs, two important assumptions of the K41 theory have been tested in the case of turbulent Rayleigh–Bénard convection. The homogeneity hypothesis has been shown to be violated for $r/\eta > 20$. The assumption of large-scale forcing has been shown to be very crude, since buoyancy forcing remains important at all non-dissipative scales of the simulation, even though the effective Bolgiano length is comparable to the depth of the convective layer. It has thus been argued that the absence of scaling behaviour in turbulent convection at $Ra=10^6$ was mostly related to these effects, and that in the ideal situation of a homogeneous flow at $Re_\lambda=30$ forced on large scales only, inertial range scalings should be observed. There, is however, a possible supplementary cause for the apparent lack of inertial range scalings in turbulent flows, namely anisotropy. This has been demonstrated by Arad *et al.* (1999*a*) for the channel flow and will be demonstrated in this paragraph for Rayleigh–Bénard convection. An important remark is that in mildly turbulent numerical simulations,

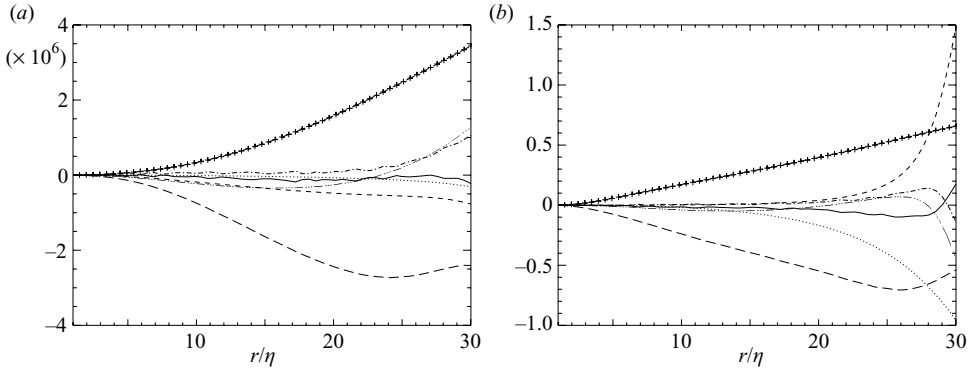

FIGURE 15. (*a*) Equation (2.15) for $\ell = 2$ with $\langle U_R\rangle_0^\ell$ (— — —), $-(\ell(\ell+1)/r^2)\int_0^r y\langle U_S\rangle_0^\ell \,\mathrm{d}y$ (+), $-(2/r^2)\int_0^r y^2[\langle\varepsilon\rangle + \langle\varepsilon'\rangle]_0^\ell \,\mathrm{d}y$ (· · ·), buoyancy term (- - -), viscous term (- · -), $\langle NH\rangle_0^\ell$ (— · · · —) and net budget (———). (*b*) Equation (2.16) for $\ell = 2$ with $\langle\Theta_R\rangle_0^\ell$ (— — —), $-(\ell(\ell+1)/r^2)\int_0^r y\langle\Theta_S\rangle_0^\ell \,\mathrm{d}y$ (+), $-(2/r^2)\int_0^r y^2[\langle N\rangle + \langle N'\rangle]_0^\ell \,\mathrm{d}y$ (· · ·), mean temperature advection term (- - -), diffusion term (- · -), $\langle NH^\theta\rangle_0^\ell$ (— · · · —) and net budget (———). $\ell = 2$.

anisotropy may be caused by different effects. It may be due to physical effects such as spherical symmetry breaking by gravity or the presence of horizontal plates in the system, as outlined in § 1, but may also be related to the fact that simulations are done in Cartesian boxes that break the rotational symmetry too. This phenomenon has been pointed out by Biferale, Gualtieri & Toschi (2000), who have shown that the projections of structure functions on anisotropic components were non-vanishing for a DNS of homogeneous isotropic turbulence performed in a Cartesian domain. These various effects are difficult to disentangle. In order to quantify the exact contribution of spurious numerical anisotropy, it would be necessary to perform statistical analyses at much higher resolutions which, as mentioned in § 3, is unfortunately not feasible currently. In every numerical study of anisotropic effects in turbulence, one should therefore keep in mind that spurious effects are present and consider the results with some caution.

The analysis is restricted to the central plane $z = 1/2$. The largest order ℓ considered in this paragraph is 6, for statistical convergence reasons. The scale-by-scale budgets for the anisotropic degrees read

$$-\langle U_R\rangle_0^\ell + \frac{\ell(\ell+1)}{r}\langle U_S\rangle_0^\ell + \frac{2\alpha g}{r^2}\int_0^r y^2\langle\Delta u_z\Delta\theta\rangle_0^\ell \,\mathrm{d}y + 2\nu\frac{\partial}{\partial r}\langle(\Delta u_i)^2\rangle_0^\ell$$
$$-\frac{2\nu\,\ell(\ell+1)}{r^2}\int_0^r\langle(\Delta u_i)^2\rangle_0^\ell \,\mathrm{d}y + \langle NH\rangle_0^\ell = \frac{2}{r^2}\int_0^r y^2[\langle\varepsilon\rangle + \langle\varepsilon'\rangle]_0^\ell \,\mathrm{d}y \quad (4.4)$$

and

$$-\langle\Theta_R\rangle_0^\ell + \frac{\ell(\ell+1)}{r}\langle\Theta_S\rangle_0^\ell + \frac{2}{r^2}\int_0^r y^2\big(\langle u_z\partial_z\langle T\rangle\Delta\theta\rangle_0^\ell - \langle u_z'\partial_z'\langle T'\rangle\Delta\theta\rangle_0^\ell\big)\,\mathrm{d}y + 2\kappa\frac{\partial}{\partial r}\langle(\Delta\theta)^2\rangle_0^\ell$$
$$-\frac{2\kappa\,\ell(\ell+1)}{r^2}\int_0^r\langle(\Delta\theta)^2\rangle_0^\ell \,\mathrm{d}y + \langle NH^\theta\rangle_0^\ell = \frac{2}{r^2}\int_0^r y^2[\langle N\rangle + \langle N'\rangle]_0^\ell \,\mathrm{d}y. \quad (4.5)$$

These budgets involve extra terms related to anisotropy in comparison to equations (4.2)–(4.3). The most important ones are those containing the transverse third-order structure functions $\langle U_S\rangle_0^\ell$ and $\langle\Theta_S\rangle_0^\ell$. To illustrate this, the $\ell = 2$ component of equations (2.15)–(2.16) can be investigated in more detail (figure 15). The (positive)

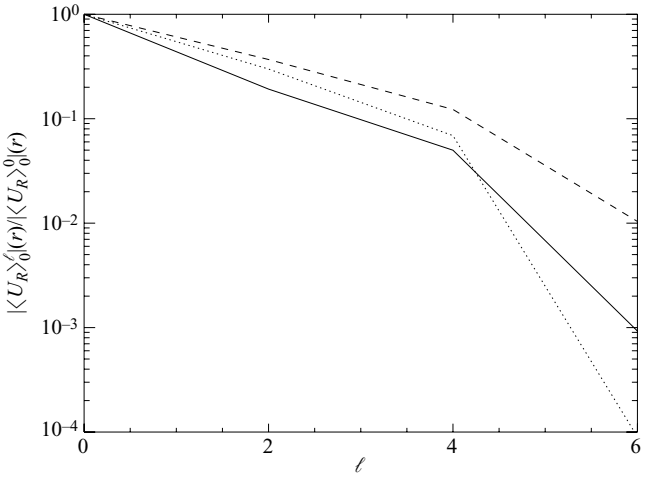

FIGURE 16. Spherical harmonics spectrum of $\langle U_R\rangle$ at the centre of the convection cell for $r/\eta = 7.9$ (———), $r/\eta = 15.3$ (· · ·) and $r/\eta = 22.6$ (- - -). Spectra are normalized with respect to $\langle U_R\rangle_0^0(r)$ for each r. The $\ell = 2$ and $\ell = 4$ terms are shown to have a comparable magnitude to the $\ell = 0$ one at moderate to large correlation lengths.

transverse third-order structure function terms are shown to compensate significantly the (negative) longitudinal third-order structure functions in each equation. There is also a small anisotropic contribution of the $[\langle\varepsilon\rangle + \langle\varepsilon'\rangle]_0^\ell$ and $[\langle N\rangle + \langle N'\rangle]_0^\ell$ terms at the largest r, which is due to increased dissipation in the boundary layers. Finally, as was the case for the isotropic equations, the inhomogeneous terms contribute to the scale-by-scale budgets in the anisotropic degrees.

Figure 16 displays the spherical harmonics spectrum of $\langle U_R\rangle_0^\ell$ for even ℓ up to $\ell = 6$ (remember that odd ℓ contributions are zero when considering averages in the central plane). It is once again emphasized that this spectrum contains contributions of both physical anisotropies due to gravity and spurious numerical anisotropies due to the use of a Cartesian computational domain. The $\ell \neq 0$ components appear to be significant in comparison to their isotropic counterpart at moderate to large correlation lengths. As the complete third-order structure functions result from a linear combination (with weights given by the spherical harmonics functions) of these various significant contributions, which may follow distinct scaling laws if foliation occurs, it is expected that genuine inertial-range scalings predicted by isotropic theories should be difficult to observe for reduced structure functions, which correspond to the complete structure functions taken at a polar angle $\theta = \pi/2$ only and therefore involve the contribution of all even spherical harmonic components of these complete structure functions evaluated at this angle. This is confirmed by figures 17 and 18; figure 17 shows a reconstruction of the reduced structure functions $\langle U_r\rangle(\theta = \pi/2)$ and $\langle\Theta_r\rangle(\theta = \pi/2)$ averaged over φ using the $\ell = 0, 2, 4, 6$ components of the complete $\langle U_r\rangle = \langle(\Delta u_i)^2 \Delta u_r\rangle$ and $\langle\Theta_r\rangle = \langle(\Delta\theta)^2 \Delta u_r\rangle$ for the present simulation. Figure 18 is a similar reconstruction of the local logarithmic slopes of the same objects. The shape and local logarithmic slopes of the reduced structure functions differ substantially from those of the $\ell = 0$ components, which shows that anisotropic components (especially $\ell = 2$, as can be seen on figure 17*a*, *b*) have a marked influence on the local scaling exponents of reduced structure functions. In the case of $\langle\Theta_r\rangle$, we find, for instance, that the local exponent of the reduced structure function for $r/\eta = 20$ is approximately 0.8, while

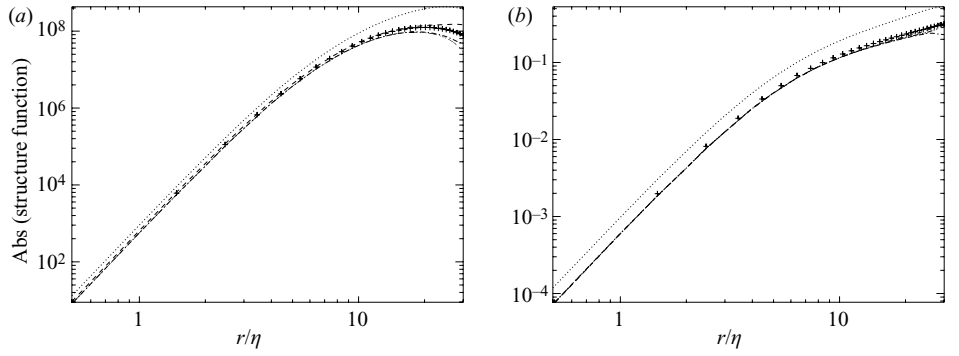

FIGURE 17. Reconstruction of the reduced structure functions $\langle U_r \rangle(\theta = \pi/2)$ ((a) + symbols) and $\langle \Theta_r \rangle(\theta = \pi/2)$ ((b) + symbols) at the centre of the convection cell using anisotropic components up to $\ell = 0$ ($\cdots$), $\ell = 2$ (- - -), $\ell = 4$ (- · -), $\ell = 6$ (— · · · —). Note the significant contribution of the $\ell = 2$ components to the reduced structure functions.

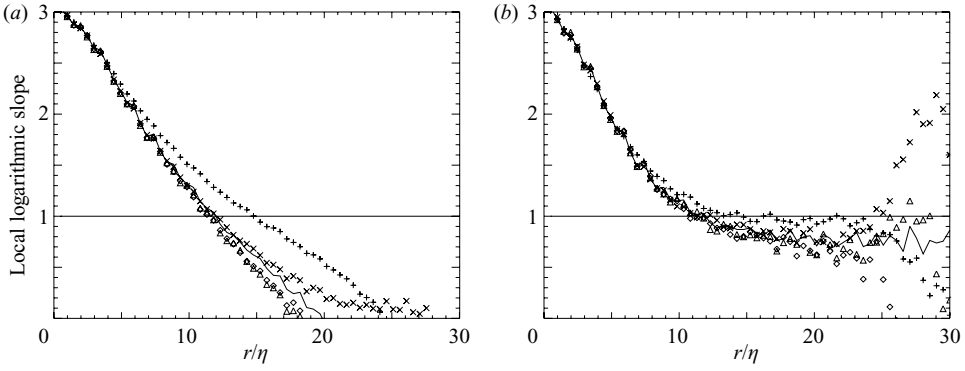

FIGURE 18. Reconstruction of the local logarithmic slope of reduced structure functions $\langle U_r \rangle(\theta = \pi/2)$ ((a) ———) and $\langle \Theta_r \rangle(\theta = \pi/2)$ ((b) ———) at the centre of the convection cell, using anisotropic components up to $\ell = 0$ (+), $\ell = 2$ (×), $\ell = 4$ (◇), $\ell = 6$ (△).

the $\ell = 0$ component exponent is 1 at the same correlation length, as shown earlier in the paper and in figure 18(b). A similar analysis stands for $\langle U_r \rangle$ (figure 18a). Such differences cannot be ignored, since they are larger than typical intermittency corrections to inertial-range scalings and than differences between concurrent theories of turbulence. Inertial-range scaling exponents obtained via an analysis of reduced structure functions should therefore be regarded with caution, at least when the flow is fully three-dimensional. For the same reasons, computations of structure functions in laboratory experiments, which rely on single-point measurements and on the Taylor hypothesis along a specific direction (that of the mean wind in Rayleigh–Bénard convection) will not necessarily lead to correct measurements of scaling exponents predicted by isotropic theories or to reliable values of intermittency corrections, because such exponents only apply to the isotropic component of the structure functions. Note, however, that the previous conclusions do not mean that measuring structure functions along a specific direction does not make physical sense. For instance, using reduced structure functions may prove useful in analysing scalings in two-dimensional flows, layered flows or in strongly anisotropic flows such as boundary layers, where scalings in the directions perpendicular to the shear can be observed. Also, in regions where the SO(3) decomposition cannot be performed, as is the case

close to walls, the only currently available methods of analysis are the computation of reduced structure functions and single-point measurements coupled to the Taylor hypothesis.

The present analysis finally proves useful to test theoretical arguments on anisotropic turbulence and the phenomenon of foliation; according to modern theories of anisotropy (Arad *et al.* 1999*b*; Biferale & Procaccia 2005), each ℓ component of structure functions may follow a distinct inertial-range scaling law with a scaling exponent increasing with ℓ. Although it proves difficult to identify scaling ranges (and therefore scaling exponents) on the $\ell \neq 0$ degrees of the third-order structure functions in this simulation, the increase of scaling exponents with ℓ seems to be qualitatively well verified, at least it is consistent with the fact that the $\ell = 2$ contribution is more important for large r than for small r in comparison to the $\ell = 0$ component. This may be viewed as an argument in favour of a small-scale return to isotropy. Note, however, that definite conclusions cannot be drawn here because the $\ell = 2$ component still remains significant for small r (figure 17). This may be a finite resolution effect related to the use of Cartesian grids and boxes that do not have rotational symmetry.

5. Summary and discussion

New results on inertial-range scaling laws, scale-by-scale budgets and correlation functions in turbulent Rayleigh–Bénard convection at moderate Rayleigh and Reynolds numbers have been reported in this paper. A derivation of generalized Kolmogorov and Yaglom equations (2.15)–(2.16), which notably makes use of the SO(3) decomposition of statistical averages, has first been presented. The formalism provides a convenient way of disentangling inhomogeneous and anisotropic effects in convective turbulence, but it can also be used to study other anisotropic and/or inhomogeneous numerically simulated or experimental flows. For this purpose, the buoyancy forcing term in the velocity equation should be replaced by any appropriate anisotropic forcing mechanism.

The analysis of scale-by-scale budgets in a convection DNS at $Ra = 10^6$ has led to the following conclusions. First of all, a compensation effect between the classical $-(4/3)\langle\varepsilon\rangle r$ term of the generalized Kolmogorov equation on one hand, inhomogeneous terms, viscous terms and buoyancy forcing on the other hand, has been demonstrated in the isotropic sector of the velocity equation. Buoyancy is the most important of these three terms. This compensation effect prevents any clear scaling law from showing up at $Re_\lambda = 30$ in the case of the third-order velocity structure function. Also, equation (1.1) has been shown to underestimate significantly the effective value of the Bolgiano length, at least for convective flows in moderate aspect ratio containers. The analysis of the mixed temperature structure function $\langle\Theta_R\rangle_0^0$ has revealed a scaling behaviour compatible with both K41 and BO59 theories in the central plane, in spite of the presence of inhomogeneous effects on large scales. Meanwhile, neglecting the term related to advection of the mean temperature profile, which is required in the BO59 theory, has been shown to be justified. Scale-by-scale budgets computed off the central plane have led to similar conclusions. An interesting inhomogeneous effect at $z = 1/4$ is the significant contribution of pressure diffusion normal to the bottom wall.

A spherical harmonics spectrum of structure functions has finally revealed that the low ℓ degree contributions to the third-order structure functions are not small in comparison to their isotropic counterparts at moderate to large scales. It has particularly been shown that using reduced structure functions at fixed polar angle in the bulk of a convection cell in order to reveal scaling behaviour predicted by isotropic

theories is misleading, since these structure functions involve linear combinations of various ℓ components which scale differently with respect to r. This argument also indicates that using single-point measurements in the bulk of three-dimensional flows together with the Taylor hypothesis in the particular direction of a mean flow to test the predictions of asymptotic dimensional isotropic theories of turbulence or to calculate intermittency corrections to these theories may lead to significant bias. It has, however, been outlined that using reduced structure functions may still be appropriate when the direction along which these functions are computed has a special importance, as is the case, for instance, in layered flows or boundary layers. Also, it has been pointed out that spurious anisotropies related to the use of Cartesian domains in simulations of mildly turbulent flows, which are difficult to quantify, certainly interfere with the genuine anisotropic effects due to gravity. Thus, the respective amplitudes of the various ℓ components of structure functions at moderate Reynolds number have to be considered with some caution. Independently of the problem of the origin of anisotropies, these results confirm the analysis of Arad *et al.* (1999*a*) for the channel flow: disentangling anisotropic effects cannot be avoided if we want to study the scaling behaviour of anisotropic systems correctly. Besides, even though the study of the r-dependence of different ℓ components in equations (2.15)–(2.16) seems to indicate qualitatively small-scale return to isotropy in the case of Rayleigh–Bénard convection, it cannot be ruled out that anisotropic effects persist at small scales, even at very high Reynolds numbers. Small-scale anisotropies (called 'ramp-cliff structures') have for instance been reported in studies of turbulent mixing of passive scalars (Mestayer *et al.* 1976; Antonia & Van Atta 1978, see also Warhaft 2000).

An important issue is to what extent the present results can be used to infer scaling behaviour at very high Rayleigh and Reynolds numbers. The still important contribution of buoyancy forcing to the scale-by-scale budget at scales smaller than L_B naturally raises the question of how many scale decades are required in a turbulent convective flow in order to be able to identify definite scalings. In the soft turbulence regime, where $Nu \sim Ra^{\gamma}$ with $1/4 < \gamma < 1/3$ (Grossmann & Lohse 2000), the Bolgiano length should not depend significantly on Ra. For instance, following equation (1.1), $L_B \sim Ra^{-3/28}$ is obtained for $\gamma = 2/7$ (Procaccia & Zeitak 1989). In the hard regime where it has been shown that $Nu \sim (RaPr)^{1/2}$ (Calzavarini *et al.* 2005), the Bolgiano length should remain constant (with respect to both Ra and Pr in that case, while the Pr dependence in the hard turbulence regime depends on whether $Pr > 1$ or $Pr < 1$), thus leading to the same result at all Rayleigh numbers. For the present aspect ratio and Prandtl number, L_B should therefore remain close to 1 at all Rayleigh numbers. On the contrary, the ratio between the dissipation scale and the effective Bolgiano scale is expected to increase with increasing Rayleigh number, which should, in principle, help to observe K41 scalings if $\eta \ll r \ll L_B$ can be achieved (Grossmann & L'vov 1993). One should, however, derive more precise conditions of applicability of K41 in that case. Assuming K41 to be valid for $r \leqslant L_B$, the buoyancy term, which equals the $-(4/3)\langle\varepsilon\rangle r$ term at L_B, would scale as $r^{5/3}$ in that range. This approximation looks rather crude for r close to L_B, but as the buoyancy term should scale as $r^{9/5}$ above L_B according to BO59, the actual local scaling exponent close to L_B may not be very different from this 5/3 value. The important point here is that this exponent be larger than 1 (which is the exponent of the $-(4/3)\langle\varepsilon\rangle r$ term). According to these scalings, non-dissipative scales as small as $3 \times 10^{-2} L_B$ should be available in order for the buoyancy term to become ten times smaller than the $-(4/3)\langle\varepsilon\rangle r$ term, which roughly corresponds to the conditions of the present simulation, in which no definite

K41 plateau can be observed (figure 5). In order to find a range of scales in which the buoyancy term would become at least one hundred times smaller than the $-(4/3)\langle\varepsilon\rangle r$ term, one should then look for a regime where $\eta < 10^{-3}L_B$. The required Rayleigh number can be evaluated by using $\eta \sim Ra^{-9/28}$, proposed by Grossmann & Lohse (1993). This relation can be calibrated using the results of the present simulation at $Ra = 10^6$, for which $\eta = 0.016$. One finally finds that Ra has to exceed several times 10^9 to obtain a flow with $\eta < 10^{-3}L_B$. Even in this situation, definite scalings are expected only in the subrange $10\eta < r < 0.1L_B$, that is over one decade. The main problem is that two scale separations $r \ll L_B$ and $r \gg \eta$ must simultaneously be satisfied, which can only occur at very high Rayleigh number. This is an important argument in understanding why inertial range scalings have been difficult to identify in experimental or numerical turbulent convection studies.

For these reasons, it is probable that various results on scaling exponents obtained in the range $10^6 < Ra < 10^9$ (e.g. Calzavarini *et al.* 2002, who have computed local scaling exponents from reduced structure functions) are biased simultaneously by anisotropic effects and significant buoyancy forcing at $r < L_B$. The lack of complete K41 or BO59 scalings in the simulations at very high Rayleigh number (up to $Ra = 2 \times 10^{11}$) of Verzicco & Camussi (2003) may also be a hint that inertial-range scalings in anisotropic flows such as Rayleigh–Bénard convection cannot be understood easily using isotropic theories. If inhomogeneity and isotropy were to play an important role in the scaling behaviour of very high Rayleigh number convective turbulence, the present results could serve as guidelines to study them in detail. More generally, the SO(3) decomposition of structure functions appears to be a very powerful (and necessary) tool to study various anisotropic flows. It should be particularly helpful to use it when possible in research domains such as astrophysics or atmospheric sciences, where anisotropic turbulence is ubiquitous. Such an investigation for strongly stratified non-Boussinesq turbulent convection, which is relevant to the Sun and other stars, is currently underway.

The author acknowledges several fruitful discussions with A. A. Schekochihin and thanks F. Anselmet, F. Lignières and M. Rieutord for many insightful comments and criticisms on early versions of the manuscript. Numerical simulations have been performed on the IBM SP4 supercomputer of Institut du Développement et des Ressources en Informatique Scientifique (IDRIS, Orsay, France), which is gratefully acknowledged.

REFERENCES

Antonia, R. & Van Atta, C. 1978 Structure functions of temperature fluctuations in turbulent shear flows. *J. Fluid Mech.* **84**, 561–580.

Antonia, R. A., Ould-Rouis, M., Anselmet, F. & Zhu, Y. 1997 Analogy between predictions of Kolmogorov and Yaglom. *J. Fluid Mech.* **332**, 395–409.

Arad, I., Biferale, L., Mazzitelli, I. & Procaccia, I. 1999*a* Disentangling scaling properties in anisotropic and inhomogeneous turbulence. *Phys. Rev. Lett.* **82**, 5040–5043.

Arad, I., L'vov, V. & Procaccia, I. 1999*b* Correlation functions in isotropic and anisotropic turbulence: the role of the symmetry group. *Phys. Rev.* E **59**, 6753–6765.

Benzi, R., Ciliberto, S., Tripiccione, R., Baudet, C., Massaioli, F. & Succi, S. 1993 Extended self-similarity in turbulent flows. *Phys. Rev.* E **48**, 29.

Benzi, R., Tripiccione, R., Massaioli, F., Succi, S. & Ciliberto, S. 1994 On the scaling of the velocity and temperature structure functions in Rayleigh–Bénard convection. *Europhys. Lett.* **25**, 341–346.

Benzi, R., Toschi, F. & Tripiccione, R. 1998 On the heat transfer in Rayleigh–Bénard systems. *J. Stat. Phys.* **93**.

Biferale, L. & Procaccia, I. 2005 Anisotropy in turbulent flows and in turbulent transport. *Phys. Rep.* **414**, 43.

Biferale, L., Gualtieri, P. & Toschi, F. 2000 Statistics of pressure and of pressure–velocity correlations in isotropic turbulence. *Phys. Fluids* **12**, 1836.

Biferale, L., Calzavarini, E., Toschi, F. & Tripiccione, R. 2003 Universality of anisotropic fluctuations from numerical simulations of turbulent flows. *Europhys. Lett.* **64**, 461–467.

Bolgiano, R. 1959 Structure of turbulence in stratified media. *J. Geophys. Res.* **64**, 2226.

Califano, F. 1996 A numerical algorithm for geophysical and astrophysical inhomogeneous fluid flows. *Comput. Phys. Comm.* **99**, 29.

Calzavarini, E., Toschi, F. & Tripiccione, R. 2002 Evidences of Bolgiano scaling in 3D Rayleigh–Bénard convection. *Phys. Rev.* E **66**, 016304.

Calzavarini, E., Lohse, D., Toschi, F. & Tripiccione, R. 2005 Rayleigh and Prandtl number scaling in the bulk of Rayleigh–Bénard turbulence. *Phys. Fluids* **17**, 055107.

Casciola, C. M., Gualtieri, P., Benzi, R. & Piva, R. 2003 Scale-by-scale budget and similarity laws for shear turbulence. *J. Fluid Mech.* **476**, 105–114.

Cattaneo, F., Brummell, N. H., Toomre, J., Malagoli, A. & Hurlburt, N. E. 1991 Turbulent compressible convection. *Astrophys. J.* **370**, 282–294.

Cattaneo, F., Lenz, D. & Weiss, N. 2001 On the origin of the solar mesogranulation. *Astrophys. J.* **563**, L91–L94.

Chandrasekhar, S. 1961 *Hydrodynamic and Hydromagnetic Stability*. Dover.

Chillá, F., Ciliberto, S., Innocenti, C. & Pampaloni, E. 1993 Boundary layer and scaling properties in turbulent thermal convection. *Nuovo Cimento* **15D**, 1229.

Ching, E. S. C., Chui, K. W., Shang, X.-D., Qiu, X.-L., Tong, P. & Xia, K.-Q. 2004 Velocity and temperature cross-scaling in turbulent thermal convection. *J. Turb.* **5**.

Danaila, L., Anselmet, F., Zhou, T. & Antonia, R. A. 1999 A generalization of Yaglom's equation which accounts for the large-scale forcing in heated decaying turbulence. **391**, 359–372.

Danaila, L., Anselmet, F., Zhou, T. & Antonia, R. A. 2001 Turbulent energy scale budget equations in a fully developed channel flow. *J. Fluid Mech.* **430**, 87–109.

Demuren, A. O., Wilson, R. V. & Carpenter, M. 2001 Higher-order compact schemes for numerical simulation of incompressible flows. Part I: theoretical development. *Numer. Heat Transfer* **39**, 207–230.

Grossmann, S. & Lohse, D. 1993 Characteristic scales in Rayleigh–Bénard turbulence. *Phys. Lett. A* **173**, 58.

Grossmann, S. & Lohse, D. 2000 Scaling in thermal convection: a unifying theory. *J. Fluid Mech.* **407**, 27.

Grossmann, S. & L'vov, V. 1993 Crossover of spectral scaling in thermal turbulence. *Phys. Rev.* E **47**, 4161.

Hartlep, T., Tilgner, A. & Busse, F. H. 2003 Large scale structures in Rayleigh–Bénard convection at high Rayleigh numbers. *Phys. Rev. Lett.* **91**, 064501.

Heslot, F., Castaing, B. & Libchaber, A. 1987 Transitions to turbulence in helium gas. *Phys. Rev.* A **36**, 5870–5873.

Hill, R. J. 1997 Applicability of Kolmogorov's and Monin's equations of turbulence. *J. Fluid Mech.* **353**, 67–81.

Hill, R. J. 2002 The approach of turbulence to the locally homogeneous asymptote as studied using exact structure–function equations. *arXiv:physics/0206034*.

Kolmogorov, A. N. 1941 Dissipation of energy in locally isotropic turbulence. *Dokl. Akad. Nauk SSSR* **32**, 16.

Lele, S. K. 1992 Compact finite difference schemes with spectral-like resolution. *J. Comput. Phys.* **103**, 16–42.

Lindborg, E. 1996 A note on Kolmogorov's third-order structure–function law, the local isotropy hypothesis and the pressure–velocity correlation. *J. Fluid Mech.* **326**, 343–356.

L'vov, V. S. 1991 Spectra of velocity and temperature fluctuations with constant entropy flux of fully developed free-convective turbulence. *Phys. Rev. Lett.* **67**, 687–690.

Mestayer, P., Gibson, C. H., Coantic, M. & Patel, A. 1976 Local anisotropy in heated and cooled turbulent boundary layers. *Phys. Fluids* **19**, 1279–1287.

Monin, A. S. & Yaglom, A. M. 1975 *Statistical Fluid Mechanics*, vol. 2. MIT Press.

Obukhov, A. M. 1959 *Dokl. Akad. Nauk. SSR* **125**, 1246.

Parodi, A., von Hardenberg, J., Passoni, G., Provenzale, A. & Spiegel, E. A. 2004 Clustering of plumes in turbulent convection. *Phys. Rev. Lett.* **92**, 194503.

Procaccia, I. & Zeitak, R. 1989 Scaling exponents in nonisotropic convective turbulence. *Phys. Rev. Lett.* **62**, 2128.

van Reeuwijk, M., Jonker, H. J. J. & Hanjalic, K. 2005 Identification of the wind in Rayleigh–Bénard convection. *Phys. Fluids* **17**, 051704.

Rincon, F., Lignières, F. & Rieutord, M. 2005 Mesoscale flows in large aspect ratio simulations of turbulent compressible convection. *Astron. Astrophys.* **430**, L57–L60.

Toomre, J., Brummell, N., Cattaneo, F. & Hurlburt, N. E. 1990 Three-dimensional compressible convection at low Prandtl numbers. *Comput. Phys. Commun.* **59**, 105–117.

Verzicco, R. & Camussi, R. 2003 Numerical experiments on strongly turbulent thermal convection in a slender cylindrical cell. *J. Fluid Mech.* **477**, 19–49.

Warhaft, Z. 2000 Passive scalars in turbulent flows. *Annu. Rev. Fluid Mech.* **32**, 203–240.

Yakhot, V. 1992 4/5 Kolmogorov law for statistically stationary turbulence: application to high-Rayleigh-number Bénard convection. *Phys. Rev. Lett.* **69**, 769.